JGR Oceans

RESEARCH ARTICLE
10.1029/2020JC016899

Modeled Three-Dimensional Currents and Eddies on an Alongshore-Variable Barred Beach

Christine M. Baker[1], Melissa Moulton[2], Britt Raubenheimer[3], Steve Elgar[3], and Nirnimesh Kumar[1]

[1]Department of Civil & Environmental Engineering, University of Washington, Seattle, WA, USA, [2]Applied Physics Laboratory, University of Washington, Seattle, WA, USA, [3]Woods Hole Oceanographic Institution, Woods Hole, MA, USA

Key Points:

- Trends in Simulating WAves till SHore (SWASH)-simulated nearshore circulation patterns and magnitudes on an alongshore-variable barred beach are similar to observations
- Small length-scale eddies are intensified by wave directional spread, and large eddies are enhanced by alongshore bathymetric variability
- Eddy length scales and low-frequency currents are weakly vertically dependent in the outer surf zone and depth-uniform in shallower water

Correspondence to:
C. Baker,
cmbaker9@uw.edu

Citation:
Baker, C. M., Moulton, M., Raubenheimer, B., Elgar, S., & Kumar, N. (2021). Modeled three-dimensional currents and eddies on an alongshore-variable barred beach. *Journal of Geophysical Research: Oceans*, *126*, e2020JC016899. https://doi.org/10.1029/2020JC016899

Received 29 OCT 2020
Accepted 22 JUN 2021

Abstract Circulation in the nearshore region, which is critical for material transport along the coast and between the surf zone and the inner shelf, includes strong vortical motions. The horizontal length scales and vertical structure associated with vortical motions are not well documented on alongshore-variable beaches. Here, a three-dimensional phase-resolving numerical model, Simulating WAves till SHore (SWASH), is compared with surfzone waves and flows on a barred beach, and is used to investigate surfzone eddies. Model simulations with measured bathymetry reproduce trends in the mean surfzone circulation patterns, including alongshore currents and rip current circulation cells observed for offshore wave heights from 0.5 to 2.0 m and incident wave directions from 0 to 15° relative to shore normal. The length scales of simulated eddies, quantified using the alongshore wavenumber spectra of vertical vorticity, suggest that increasing wave directional spread intensifies small-scale eddies ($\mathcal{O}$(10) m). Simulations with bathymetric variability ranging from alongshore uniform to highly alongshore variable indicate that large-scale eddies ($\mathcal{O}$(100) m) may be enhanced by surfzone bathymetric variability, whereas small-scale eddies ($\mathcal{O}$(10) m) are less dependent on bathymetric variability. The simulated vertical dependence of the magnitude and mean length scale (centroid) of the alongshore wavenumber spectra of vertical vorticity and very low-frequency ($f \approx 0.005$ Hz) currents is weak in the outer surf zone, and decreases toward the shoreline. The vertical dependence in the simulations may be affected by the vertical structure of turbulence, mean shear, and bottom boundary layer dynamics.

Plain Language Summary The nearshore region includes the surf zone, where waves break, and the inner shelf, which extends several km offshore from the surf zone. Within this region, currents transport contaminants, sediments, and larvae along the coast and between the beach and the shelf. Nearshore eddies are rotational currents that fluctuate at timescales longer than individual waves and shorter than mean hourly currents, and are important to mixing and transport. Here, a three-dimensional numerical model simulates observed waves and flow patterns on a natural beach near Duck, NC with highly variable seafloor elevations (e.g., bumps and holes). Estimates of the alongshore (parallel to the coastline) length of simulated eddies suggest that large eddies are enhanced by higher variability in the seafloor, whereas the intensity of small eddies increases when waves enter the surf zone with larger directional spread (from multiple directions). The structure and strength of nearshore eddies over the water column is shown to vary across the surf zone.

1. Introduction

The nearshore region consists of the surf zone, extending from the shoreline to the seaward limit of depth-induced wave breaking, and the inner shelf, a region with overlapping surface and bottom boundary layers on the continental shelf offshore of the surf zone (Lentz & Fewings, 2012). Quantifying circulation dynamics and the transport of material (e.g., contaminants, sediments, and larvae) in the nearshore is critical given the concentration of recreational, commercial, and ecosystem resources in this region (Boehm et al., 2017). Nearshore currents may dilute or concentrate pollutants and pathogens that cause gastrointestinal infections and require beach closures (Stoner & Dorfman, 2007), and excess nutrient supply from terrestrial runoff may lead to eutrophication in coastal zones, creating hypoxic conditions that threaten benthic organisms and ecosystem health (Boehm et al., 2016). In addition, species inhabiting the nearshore (e.g., intertidal invertebrate gametes) exploit cross-shore circulation for recruitment and settlement (Morgan et al., 2018;

Shanks et al., 2010). A comprehensive understanding of nearshore dynamics is necessary to maintain public safety and reduce anthropogenic stresses on ecosystems.

Surf zone circulation is the result of complex interactions between surface waves, bathymetric irregularities, and bottom boundary layer dynamics. Mean cross-shore velocities are characterized by a balance between radiation-stress gradients, barotropic-pressure gradients, and a weaker contribution from bottom stress, resulting in wave setup and an offshore near-bed return current (i.e., "undertow," Bowen et al., 1968; Longuet-Higgins & Stewart, 1964; Raubenheimer et al., 2001; Stive & Wind, 1982). Wave-induced mean alongshore currents result from alongshore barotropic-pressure gradients (Apotsos et al., 2008; Hansen et al., 2015) and cross-shore gradients of the off-diagonal component of the radiation-stress tensor (Feddersen et al., 1998; Garcez-Faria et al., 1998; Longuet-Higgins, 1970), primarily balanced by bottom stress (Visser, 1986; Simons et al., 1992; Reniers, Thornton, et al., 2004). Wave breaking over alongshore bathymetric variations drives rip currents and meandering alongshore currents, including cell-like circulation patterns (Castelle et al., 2016; Dalrymple et al., 2011; MacMahan et al., 2006; Moulton et al., 2017).

The vertical structure of surfzone currents depends on the forces associated with surface wave breaking, bottom friction, and interaction with the three-dimensional circulation (MacMahan et al., 2004; Putrevu et al., 1995), and is altered by the vertical distribution of turbulence in the water column, which depends on the breaking wave energy and bed roughness (Feddersen, 2012; Feddersen & Trowbridge, 2005; Henderson et al., 2017). Field and numerical modeling studies have investigated the vertical profile of undertow (Garcez-Faria et al., 1998) and of mean alongshore currents (Garcez-Faria et al., 2000; Reniers, Thornton, et al., 2004). However, the three-dimensional structure of surf zone velocities at timescales longer than those of wind waves (e.g., surf zone eddies) and their implications for material exchange are not understood well.

Surf zone eddy activity contributes to dispersion and mixing, thus affecting the transport of material along the coast and between the surf zone and the inner shelf (Clark et al., 2010, 2011; Spydell & Feddersen, 2009; Suanda & Feddersen, 2015). Very low-frequency (VLF) vortical motions at timescales greater than 250 s (approximately $f < 0.004$ Hz, where f is frequency), longer than infragravity timescales ($0.004 < f < 0.040$ Hz), may be generated by shear instabilities (Allen et al., 1996; Bowen & Holman, 1989; Oltman-Shay et al., 1989) and wave-breaking induced vorticity (Haller et al., 1999; Peregrine, 1998). Shear instabilities in a wave-driven alongshore current have been observed with length scales up to several hundred meters (Oltman-Shay et al., 1989). Wave-group driven alongshore radiation stress gradients from alongshore wave-breaking variability may contribute to surf zone eddy generation with length scales on the order ($\mathcal{O}$) of 100 m (Haller et al., 1999; Long & Özkan Haller, 2009; Reniers, Roelvink, & Thornton, 2004). As a result of alongshore gradients in wave dissipation, short-crested breaking waves generate vorticity with length scales $\mathcal{O}(10)$ m (Clark et al., 2012; Peregrine, 1998), which are hypothesized to coalesce to larger scales $\mathcal{O}(100)$ m (Elgar & Raubenheimer, 2020; Spydell & Feddersen, 2009) due to an inverse energy cascade (Boffetta & Ecke, 2012; Kraichnan, 1967). The length scales associated with vortical motions generated by both shear instabilities and wave breaking have been explored for depth-integrated velocities on alongshore-uniform beaches (Feddersen, 2014; Feddersen et al., 2011; Kumar & Feddersen, 2017; Spydell & Feddersen, 2009) and an alongshore-varying beach (O'Dea et al., 2021), but have not been explored for depth-varying velocities on beaches with complex bathymetry.

Surf zone vortical motions, often assumed to be depth-uniform, usually have been measured at a single elevation with a horizontally spaced sensor array. However, two recent studies on a barred beach measured low-frequency motions with vertically stacked electromagnetic current sensors (Lippmann et al., 2016) and acoustic Doppler profilers (Henderson et al., 2017). These studies found that low-frequency cross- and alongshore velocities are weakly vertically dependent in the outer surf zone (Henderson et al., 2017; Lippmann et al., 2016). Analytic solutions based on bottom boundary layer theory indicate complex vertical structure of low-frequency motions in the presence of a horizontally sheared alongshore current (Lippmann & Bowen, 2016). Although these studies have established that eddies in the outer surf zone have some vertical variability, further investigation is necessary to understand the vertical dependence of VLF currents for varying beach profiles and wave conditions.

Numerical modeling has been used to investigate the three-dimensionality of surf zone vortical motions. Phase-averaged models that simulate the evolution of the wave energy spectrum are skillful at reproducing some mean wave-induced dynamics, including rip-current circulation, alongshore currents, and wave setup (Kumar et al., 2012; Reniers, Thornton, et al., 2004; Uchiyama et al., 2010), but do not include vertical vorticity generated by finite-crested wave breaking. Studies using three-dimensional phase-averaged model simulations indicate that vertical shear instabilities modify depth-dependent currents due to dispersive mixing (Newberger & Allen, 2007a, 2007b), and that VLF motions are excited on complex bathymetry (Uchiyama et al., 2017). However, the parameterizations of wave-induced vorticity associated with energy dissipation from short-crested wave breaking used in phase-averaged models have not been tested extensively.

Coupled ocean-circulation and phase-averaged wave models (e.g., COAWST) simulate vertically varying surf zone circulation (Warner et al., 2010; Kumar et al., 2012), and can be one-way coupled with depth-averaged phase-resolving models (e.g., funwaveC) to allow for the investigation of three-dimensional eddies resulting from bulk vorticity injection similar to that resulting from short-crested wave breaking (Kumar & Feddersen, 2017). However, wave-forced rotational flows associated with eddies may be aliased as a result of the 1 Hz model output from the phase-resolving simulations (Kumar & Feddersen, 2017). In addition, two-way coupled wave-current interactions between three-dimensional eddies and propagating waves are not included.

Phase-resolving Boussinesq models (e.g., FUNWAVE-TVD and funwaveC), which simulate individual wave propagation, have been used to study surf zone vorticity dynamics, including finite-crested wave-breaking eddy generation (Feddersen, 2014; Hally-Rosendahl & Feddersen, 2016). These models are depth integrated, and thus do not resolve eddy vertical variability. Three-dimensional phase-resolving non-hydrostatic numerical models, such as Simulating WAves til SHore (SWASH) and NHWAVE, contain the physics needed to simulate three-dimensional circulation and vorticity dynamics, including wave-forced eddy generation (Derakhti et al., 2016; Zijlema et al., 2011). SWASH has been used to study nearshore wave breaking, infragravity wave dynamics, nonlinear infragravity-wave interactions, run-up oscillations, and nonlinear wave-dynamics (de Bakker et al., 2016; Rijnsdorp et al., 2012, 2014; Ruju et al., 2014; Smit et al., 2014, 2013). Although SWASH has skill simulating wave-induced flows measured in the laboratory, including the undertow profile and alongshore currents (Rijnsdorp et al., 2017), the accuracy of SWASH-simulated surf zone circulation on an alongshore-variable beach has not been tested.

Here, SWASH is used to simulate three-dimensional wave propagation and circulation on a beach with complex alongshore-varying bathymetry. The field experiment and model setup are described in section 2, and the results comparing the observed with the simulated wave statistics and circulation patterns are presented in section 3. Additionally, the relative roles of alongshore bathymetric variability and directional spread in the horizontal and depth variability of length scales of the simulated eddies, and of the vertical structure of VLF horizontal velocities, are presented in section 3. The physical processes influencing the horizontal and depth variability of surf zone eddies and VLF currents are discussed in section 4. The results are summarized in section 5.

2. Methods

2.1. Field Experiment

Field observations were collected on an alongshore-inhomogeneous barred beach near Duck, North Carolina at the United States Army Corps of Engineers Field Research Facility (FRF, http://frf.usace.army.mil/frf.shtml) as part of the BathyDuck-2015 Experiment, a large effort to evaluate and improve the estimation of surf zone bathymetry (Smith et al., 2017). Instruments included offshore wave sensors in water depths (h) of 11 (x, y = 1,295, 978 m, positive offshore and to the north, respectively) and 6 m (x, y = 606, 937 m) and an array of colocated pressure sensors and acoustic Doppler velocimeters (ADVs) in the surf zone, sampled at 2 Hz (Figures 1a and 1b). Two cross-shore transects of four colocated ADVs and pressure sensors were deployed from $-3.5 < z < -1.5$ m (positive upward and referenced to the NAVD88 datum, approximately local mean sea level), initially positioned 0.5–1.0 m above the bed, and separated by approximately 125 m in the cross-shore and 75 m in the alongshore (Figures 1a and 1b, red circles, y = 741 and 813 m). Two additional

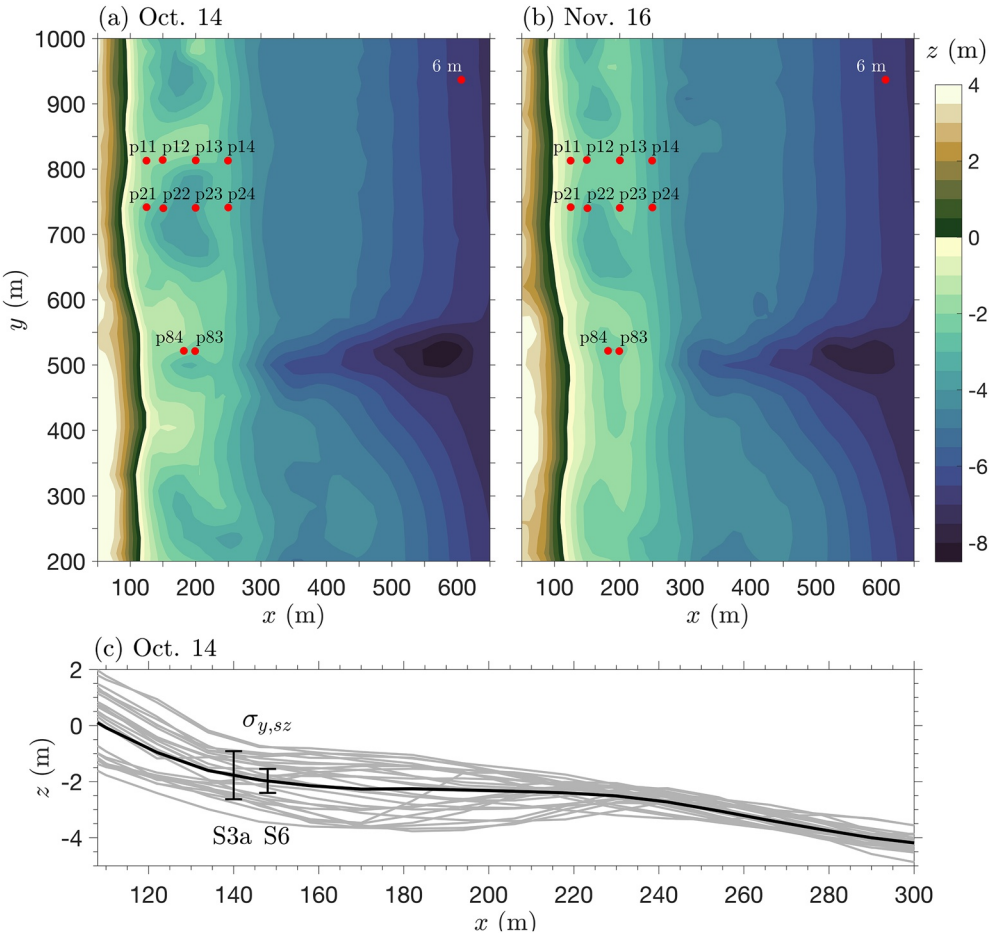

Figure 1. Locations of colocated acoustic Doppler velocimeters (ADVs) and pressure gauges (red symbols) and bathymetry (z, color contours, scale on the right) measured on (a) October 14, 2015 and (b) November 16, 2015 versus cross- (x) and alongshore (y) coordinates. Bathymetry from October and November have alongshore-varying sandbar-trough and terrace systems interrupted by channels. The deep channel at around $y = 500$ m is formed from scour near the Field Research Facility (FRF) pier. (c) Vertical elevation (z) versus cross-shore coordinate (x) for profiles every 45 m in the alongshore (S3a, gray curves) and the alongshore-averaged profile (S7, black curve) for October 14. The alongshore standard deviation of the bathymetry ($\sigma_{y,sz}$) in the surf zone is denoted with vertical bars for simulations S3a and S6 (Tables 1 and 2).

sensors were deployed south of these arrays near the FRF pier ($y = 521$ m). Occasionally, current meter data were omitted when sensors were out of the water (low tide) or buried (accretion).

Bathymetric surveys were performed on October 14 and November 16, 2015 with the Lighter Amphibious Resupply Cargo (LARC) vehicle using a single-beam acoustic sonar and RTK GPS (Figure 1). The survey data were smoothed to an 8 m cross-shore by 45 m alongshore gridded bathymetry with estimated root-mean-square vertical elevation errors of approximately 0.05 m, attributed to sampling and interpolation errors (Plant et al., 2002; Smith et al., 2017). The surveys covered 1,200 m in the alongshore ($y = -100$–1,100 m) and spanned from the beach to $h \approx 9$ m ($x = 50$–950 m).

Between the most offshore position of the shoreline ($x = 135$ m) and the bar crest ($x = 235$ m), the October 14 bathymetry has a maximum surfzone alongshore standard deviation ($\sigma_{y,sz}$) of 0.86 m (Figure 1c, left vertical bar, S3a) located in the trough region. The nondimensional metric of bathymetric nonuniformity (χ^2), the spatially averaged and normalized squared difference between the measured depth ($h(x, y)$) and the alongshore-averaged cross-shore depth ($\bar{h}(x)$) (Ruessink et al., 2001) is defined as:

$$\chi^2 = \frac{1}{L_x L_y} \int_{x_0}^{x_{sz}} \int_{y_{south}}^{y_{north}} \left(\frac{h(x,y) - \bar{h}(x)}{\bar{h}(x)} \right)^2 dy dx \quad (1)$$

where L_x and L_y are the cross-shore and alongshore length where χ^2 is evaluated. χ^2 computed from $x = 134$ m (the farthest offshore extent where $h = 0$ m, x_0) to $x = 260$ m (the edge of the surf zone for the simulations with the largest wave height, x_{sz}) and $-100 \geq y \geq 1{,}100$ m is 0.099. The χ^2 is sensitive to the cross-shore extent over which it is computed and increases for smaller surf zone widths. The χ^2 of the bathymetry observed on October 14 is ~5 times larger than previous experiments with alongshore bathymetric variations described as small to moderate in Duck, NC and central California (Ruessink et al., 2001; Feddersen & Guza, 2003; O'Dea et al., 2021), and is >25 times larger than observed on a beach described as alongshore uniform (Spydell & Feddersen, 2009). On October 14 (November 16), the average shoreline position was approximately $x = 108$ m (110 m), and a single bar was located near $x = 235$ m (215 m) with an alongshore-variable trough near $x = 175$ m (170 m). In both bathymetric surveys, the morphology includes bar-trough patterns (e.g., Figure 1a: $y = 600$–750 m, Figure 1b: $y = 550$–700 m), variable terraces (e.g., Figure 1a: $y = 750$–825 m, Figure 1b: $y = 700$–800 m), and a scoured channel under the FRF pier (Figures 1a and 1b: $y = 500$ m). Between October 14 and November 16, there was on average about a 10 m shoreward migration of the bar crest at $y = 600$–$1{,}100$ m and a southward migration of some bathymetric features, such as the depression from $y = 600$–750 m on October 14, which may have migrated to $y = 550$–700 by November 16 (Figures 1a and 1b).

ADV measurements were quality controlled (Elgar et al., 2005) and used to compute hourly bulk current and wave parameters, reported as the average of six 512 s data collections each hour. A frequency-dependent correction for depth using linear wave theory was applied to nearshore pressure measurements to estimate sea-surface elevation statistics (Guza & Thornton, 1980). Significant wave heights (H_s, 4 times the standard deviation of sea-surface elevation fluctuations for $0.05 < f < 0.30$ Hz) have an estimated error <5%. The energy-weighted wave angles (θ) and directional spread (σ_θ) were computed for the same frequency range using directional moments (Kuik et al., 1988), and have an estimated error of 5° owing to compass inaccuracies. Incident waves from counter-clockwise (from the north-east) and clockwise (from the south-east) of shore-normal are reported as $\theta > 0°$ and $\theta < 0°$, respectively. The range of the mean water level ($\langle \eta \rangle$, including tides, surge, and other large-scale water-level fluctuations) measured by a NOAA tide gauge ($h = 6$ m, $x, y = 582, 509$ m) varied from −0.6 to 1.0 m. In 11 m water depth, H_s ranged from 0.3 to 2.0 m, θ varied from −45° to 50°, σ_θ was between 25° to 40°, and the peak wave periods (T_p) ranged from 4 to 12 s. In 2 m water depth, wave heights were depth limited, and thus varied tidally, wave directions usually were close to shore-normal, and directional spreads decreased relative to offshore waves. The maximum hourly average current speeds at a nearshore sensor at $h \approx 2$ m ($x, y = 150, 740$ m), was approximately 0.5 m/s (0.6 m/s) in the cross-shore (alongshore) when $H_s > 1.5$ m.

2.2. Numerical Modeling Testing Framework

Nearshore circulation and wave propagation were simulated using SWASH, a three-dimensional open source non-hydrostatic wave-flow model (Zijlema et al., 2011). SWASH solves the nonlinear shallow water equations including non-hydrostatic pressure, and conserves temperature, salinity, and suspended sediment (Zijlema & Stelling, 2005). The second-order finite difference approximations (in time and space) in SWASH improve the computational efficiency, while correcting for frequency dispersion through the addition of more vertical layers. The steepening wave front is resolved in simulations with sufficient vertical resolution and regarded as a jump-discontinuity in the flow variables (free surface, and velocities). Conservation of momentum is enforced across the discontinuity, which enables an energy dissipation rate similar to a hydraulic jump (Smit et al., 2013). The hydrostatic front approximation that initiates wave breaking based on thresholds also is used in case the vertical gradients are not resolved adequately. Vertical mixing is approximated using a k–ϵ model, where k is the turbulent kinetic energy per unit mass and ϵ is the dissipation rate of turbulent kinetic energy per unit mass (Launder & Spalding, 1983). The sensitivity to other approaches for vertical mixing is not explored here (Rijnsdorp et al., 2017, see Appendix A for further details about the model).

Table 1
Simulated Test Cases Forced With Observed Conditions, Including Hour-Average Mean Water Elevation ($\langle\eta\rangle$) And Offshore ($h = 11$ m) Significant Wave Height (H_s), Peak Wave Period (T_p), Incident Wave Angle ($\theta = 0°$ is Shore-Normal, $\theta < 0°$ Indicates Waves From the Southeast), Directional Spread (σ_θ), and the JONSWAP Gamma Parameter (γ_J)

Sim.	Time of obs. (EDT)	Bathymetry	$\langle\eta\rangle$ (m)	H_s (m)	T_p (s)	θ (°)	σ_θ (°)	γ_J	L_{sz}
S1	Oct. 20 10:00	Oct. 14	−0.03	0.62	7.8	−3.4	30.8	1.9	70
S2	Oct. 20 15:00	Oct. 14	0.13	0.51	8.8	−15.0	29.5	1.8	58
S3a	Oct. 28 00:00	Oct. 14	−0.32	1.95	7.1	−2.1	28.6	1.4	146
S3b	Oct. 28 00:00	Nov. 16	−0.32	1.95	7.1	−2.1	28.6	1.4	134

Note. Model bathymetry for each simulation was derived from surveys on October 14 or November 16. The surf zone width (L_{sz}) is the distance between the shoreline (x_{sl}, where alongshore-averaged water depth, $\langle h\rangle_y = 0$) and the beginning of wave breaking (x_{sz}).

SWASH was run on a 2 m-resolution horizontal grid spanning 1,500 m alongshore and 900 m cross-shore from the shoreline to $h = 9$ m water depth with five vertical layers. Simulations were run with the observed bathymetry interpolated to the model grid with the still water level set to the hour-averaged observed ($h = 6$ m) water elevation ($\langle\eta\rangle$). To allow for north and south periodic boundary conditions, the domain was extended an additional 124 m alongshore on the northern and southern boundaries, converging exponentially to an alongshore-averaged bathymetry. All simulations were conducted for 2 h with an initial time step of 0.04 s and a cycle length (repeated length of the time series realization) of 1 h. After 1 h of model spin up, 1 Hz output for the second hour is used for analysis. Further information about the numerical approach and model settings are provided in Appendix A.

The model was forced uniformly along the offshore boundary by a model-generated JONSWAP spectrum based on the observed offshore bulk wave parameters (H_s, T_p, θ, and σ_θ in $h = 11$ m) and a peakedness parameter (γ_J) calibrated to match the observed spectra ($\gamma_J = 1.4$–1.9). Errors introduced by applying forcing from an 11 m depth measurement at the 9 m depth model domain boundary are estimated to be small, with refraction resulting in differences of less than 1° in direction and less than 0.01 m in wave height. Bulk wave and current statistics from model simulations with bathymetry derived from the October 14 survey (Figure 1a) are compared with observations for three directionally spread wave conditions (Table 1). Two of the simulations (S1 and S2, observed conditions on October 20 10:00 and 15:00 Eastern Daylight Time (EDT)) were selected to compare oblique with shore-normal waves during lower-energy conditions. The third simulation (S3a, observed conditions on October 28 00:00 EDT) has higher-energy, normally incident waves. Additionally, the sensitivity of the simulated nearshore circulation to bathymetry is investigated by repeating the third simulation (S3a) with bathymetry observed on November 16 (S3b, Figure 1b). The surfzone width (L_{sz}) for each simulation is the distance from the alongshore-averaged shoreline position (x_{sl}, set by the mean water elevation) to the outer edge of the surf zone (x_{sz}, beginning of breaker zone), defined as the cross-shore location with the maximum cross-shore gradient in the alongshore-averaged significant wave height, $d\left\langle H_s\right\rangle_y/dx$ (Table 1).

The numerical framework and stability of SWASH impacted the selection of the test cases. For conditions with highly oblique, directionally spread waves ($\theta > 20°$, $\sigma_\theta > 30°$), unrealistic alongshore banding of H_s resulted from interference of the limited directional components that could be included in the domain geometry. Additionally, SWASH became unstable in the swash zone for moderate-energy oblique wave conditions ($\theta > 20°$, $H_s > 1$ m). Simulations were forced with a JONSWAP spectrum generated with the bulk wave parameters, and thus time periods with bi-modal wave spectra, including from October 14 10:00 to October 17 23:00 EDT, were not simulated. The stability was compromised and computational time substantially increased when the number of vertical layers was doubled.

2.3. Vorticity Wavenumber Spectra Analysis

The alongshore length scales of surf zone eddies are quantified with the hour average of 1 Hz alongshore wavenumber spectra of vertical vorticity (with the spatial mean removed) over the second hour of a simulation (3,600–7,200 s). The alongshore wavenumber spectra were computed from depth-averaged vertical

Table 2
Simulations for the Eddy Length-Scale Analysis With the Corresponding Alongshore Bathymetry Standard Deviation in the Surf Zone ($\sigma_{y,sz}$), and the Offshore Directional Spread (σ_θ)

Sim. No.	$\sigma_{y,sz}$ (m)	σ_θ (°)
S3a	0.86	28.6
S4	0.86	14.3
S5	0.86	0
S6	0.43	28.6
S7	0	28.6

Note. All other model parameters for each run are consistent with those for S3a (Table 1).

vorticity ($S_{\omega\omega}$) and from vertical vorticity at individual elevations ($S_{\omega\omega}(z)$), for alongshore eddy length scales $L \geq 4$ m ($k/2\pi \leq 0.25$ m^{-1}, where k is the wavenumber) at each cross-shore grid location (2 m resolution). Vertical vorticity was estimated from gridded velocity components using a central-difference approach (Patankar, 1980), where vorticity at individual vertical layers was computed from horizontal velocities at time-evolving terrain-following sigma layers interpolated to a grid of fixed elevations. To estimate phase-averaged vorticity, a 60 s moving average is applied to the vertical vorticity prior to computing the wavenumber spectra of vertical vorticity at 1 Hz. The averaging is applied prior to, rather than following, the discrete vorticity estimate to remove apparent instantaneous wave-induced vorticity that is an artifact of the discretization.

Wavenumber spectra were computed for the energetic shore-normal waves (S3a) over the observed alongshore-variable bathymetry (measured October 14, Figures 1a and 1c, $\sigma_{y,sz} = 0.86$ m) and for four additional simulations (Table 2) with the same forcing as in S3a (Table 1), but with altered alongshore bathymetric variability and wave directional spread. The sensitivity of eddy length scales to the incident wave field (e.g., short-crested wave breaking) is investigated with two simulations with the observed October 14 bathymetry and with half of the observed (S4, $\sigma_\theta = 14.3°$) and zero (S5) offshore directional spread. The influence of alongshore bathymetric variability on the distribution of eddy length scales is addressed with two simulations (S6, S7) with the observed offshore directional spread ($\sigma_\theta = 28.6°$) and reduced alongshore bathymetric variability. S6 has bathymetry with half of the observed alongshore variability ($\sigma_{y,sz} = 0.43$ m, bathymetric features decreased by half the observed amplitude about the alongshore-average bathymetry, Figure 1c, right vertical bar), and S7 has alongshore-uniform bathymetry set to the alongshore-average of the observed bathymetric profiles ($\sigma_{y,sz} = 0$ m, Figure 1c, thick black curve).

2.4. Very Low-Frequency Velocity Analysis

The VLF surfzone currents, defined here as currents in the band $0.003 < f < 0.007$ Hz, were computed with 1 Hz time series along several cross-shore transects of the three-dimensional SWASH simulations. Similar to the vorticity estimates at specific elevations, horizontal velocities at sigma layers were interpolated to a fixed vertical grid spanning from near the mean sea-surface to near the bed. Velocities defined as "near-surface" are at the grid point closest to one half of the alongshore-averaged significant wave height below the mean sea-surface elevation. Velocities defined as "near-bottom" are at the grid point closest to 0.03 m above the bed, typically outside of a surface-gravity wave bottom boundary layer. Temporal velocity spectral analyses were performed using a Hanning window period of 512 s with an overlap period of 256 s for a 1 h cross- (u) and alongshore (v) velocity 1 Hz time series, yielding a $\Delta f = 0.002$ Hz with the lowest bin centered at $f = 0.002$ Hz and 28 DOF. To test the confidence in VLF statistics over the last hour of the 2 h simulation, simulation S3a and S7 (Table 2) were run for a longer time period (4 h with 84 DOF). The statistics from the last hour of the 2 h simulation (3,600–7,200 s) were similar to statistics from the last 3 h of the 4 h simulation (3,600–14,400 s), justifying that the results are statistically significant for the shorter simulation. When converted to equivalent velocity using the linear finite-depth dispersion relationship, sea-surface elevation spectral levels ($S_{\eta\eta} * g/h$ where g is gravitational acceleration and h is mean water depth) within the VLF band are 1–2 orders of magnitude lower than the velocity spectral levels ($S_{uu} + S_{vv}$, for example, modeled at $x, y = 132$, 740 m in Figure 2, dashed lines indicate the VLF band), indicating that VLF motions are rotational rather than directly forced by sea, swell, or infragravity waves (Elgar et al., 2019; Feddersen et al., 2011; Lippmann

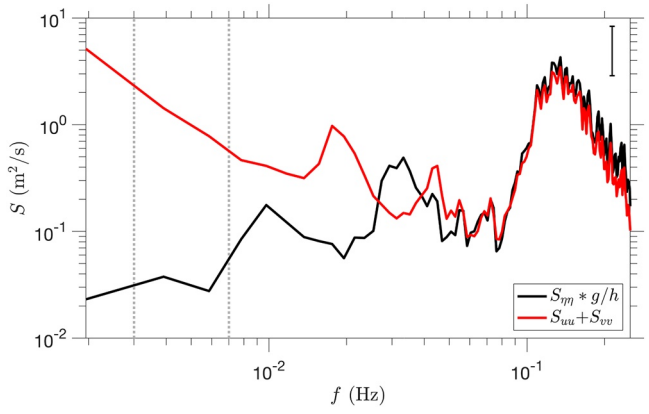

Figure 2. Sea-surface elevation spectral density converted to equivalent velocity ($S_{\eta\eta} * g/h$, black) and the sum of the depth-averaged cross- and alongshore spectral densities (S_{uu}, S_{vv}, red) in the surf zone ($x, y = 132$, 740 m) versus frequency (f). Vortical motion is the dominant energy in the Very low-frequency (VLF) band (between the vertical dashed lines). The vertical bar indicates the 95% confidence interval for 28 DOF.

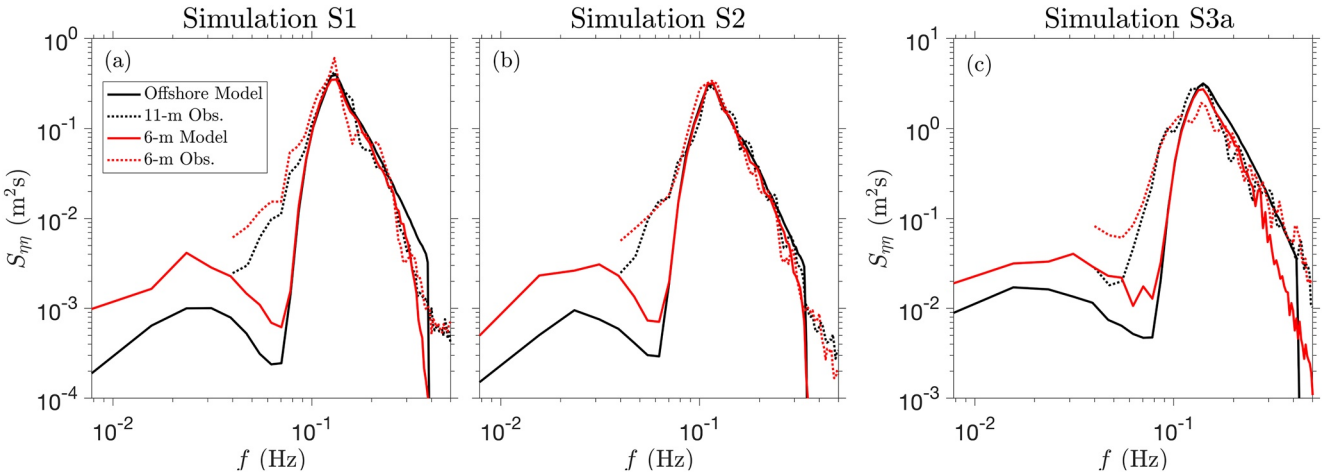

Figure 3. Sea-surface elevation spectral densities ($S_{\eta\eta}$) versus frequency (f) for alongshore-averaged model spectra at the offshore boundary (solid-black curves), observed spectra in 11 m depth (dashed-black curves), and simulated (solid-red curves) and observed (dashed-red curves) spectra in 6 m depth for simulations (a) S1, (b) S2, and (c) S3a. There are 48 DOF in the spectra.

et al., 1999; MacMahan et al., 2010). The observed and modeled velocity spectral levels at $x, y = 132, 740$ m are similar for infragravity and VLF motions (within the 95% confidence interval).

The VLF spectral densities (S_{uu}, S_{vv}) are computed as the sum of the frequency bins centered at $f = 0.004$ and 0.006 Hz. The squared coherence of the VLF velocity (λ_u^2, λ_v^2) and the phase relative to the near-surface VLF velocity (ϕ_u, ϕ_v, positive and negative phase indicate leading and lagging surface velocities) are computed as the energy weighted average over the $f = 0.004$ and 0.006 Hz bins (Hannan, 1970; Priestely, 1981). To represent the relative variability of VLF velocities over the water column, $(u_{rms} - u_{0,rms})/u_{0,rms}$ and $(v_{rms} - v_{0,rms})/v_{0,rms}$, the normalized difference between the root mean square (rms) over time of filtered VLF velocities (u_{rms}, v_{rms}) and the near-surface velocity ($u_{0,rms}$, $v_{0,rms}$), was computed from the band-passed $0.003 < f < 0.007$ Hz) velocities (PL64 filter, Rosenfeld, 1983), where greater and less than 0 indicates more and less VLF velocity variance at depth relative to near the surface, respectively.

3. Results

3.1. Observed and Modeled Nearshore Conditions

The capability of SWASH to simulate surf zone circulation on a natural beach is tested by comparing the modeled with the observed hourly bulk wave and current statistics. At the model offshore boundary ($h = 11$ m) for simulations with October 14 bathymetry (S1, S2, S3a, Table 1), the alongshore-averaged $S_{\eta\eta}$ is similar to the observed sea-surface elevation spectra ($S_{\eta\eta}$, Figure 3, black curves). The observed and modeled $S_{\eta\eta}$ also are similar at $h = 6$ m (Figure 3, red curves), with slightly lower energy in the modeled spectra at the peak frequency for lower-energy waves (S1, S2). The differences between the observed and modeled spectra at $h = 6$ m may be associated with differences in the observed and modeled offshore spectrum and boundary conditions (Figure 3, black curves), including the assumption of uniform wave forcing along the offshore boundary, and inaccuracy in modeled physics (e.g., wave transformation, wave-wave interactions, and other nonlinear processes).

The modeled and observed H_s for simulations with October 14 bathymetry (S1, S2, and S3a) have similar patterns, including a reduction in H_s from depth-limited breaking in the surf zone (Figures 4b and 4d, 5b, x_{sz}: dashed-white lines) and smaller H_s near the pier due to wave refraction (around $y = 500$ m). Although the model simulates the observed cross-shore pattern of H_s, the modeled H_s is larger than observed (RMSE = 0.28 m, bias = 0.23 m, Figures 4b and 4d, 5b, colors in circles are darker than in the surrounding area). The positive bias of the modeled H_s is smaller if the stations near the pier (p84 and p85), where large changes in bathymetry may occur, are not included in the comparison (RMSE = 0.21 m, bias = 0.18 m). The similar patterns and positive bias of modeled H_s relative to observations is shown along the cross-shore

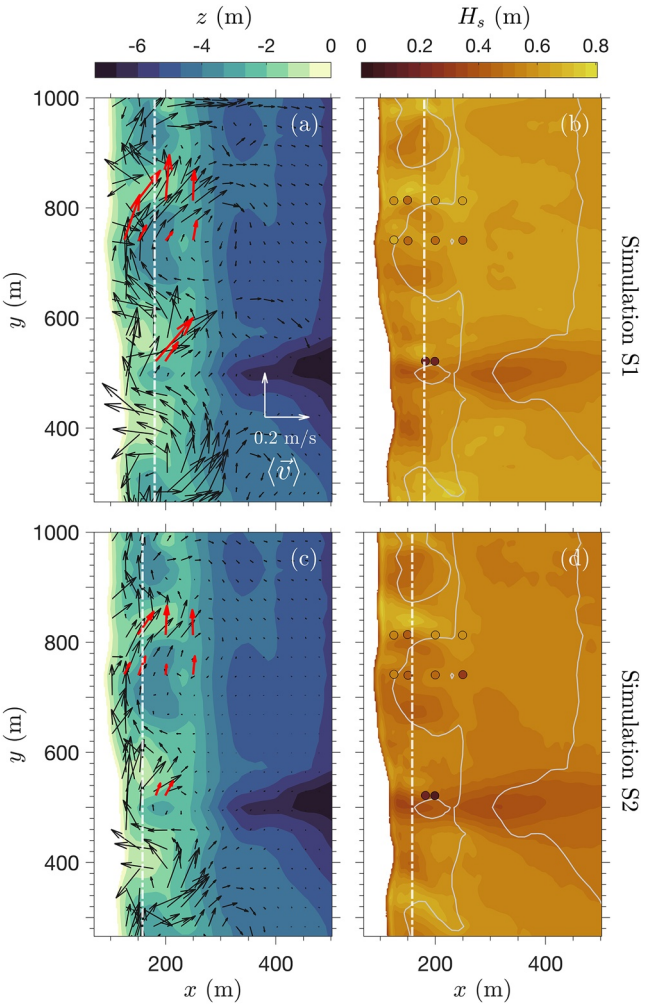

Figure 4. Observed (left: red arrows, right: filled circles) and modeled (left: black arrows, right: color contours) (a) and (c) hour-averaged depth-averaged velocity, $\langle \vec{v} \rangle$ and (b) and (d) significant wave height, H_s for small (c and d) shore-normal (S1) and (c and d) oblique (S2) wave conditions. Bathymetry (left: color contours, right: gray contour curves at 2.5 and 5.0 m depths) and the approximate outer edge of the surf zone (x_{sz}, all panels: dashed-white lines) are shown. Sensor measurements that were removed during quality control are not included here.

transect at $y = 741$ m (along stations p21-24, Figure 6a), where the modeled statistics are alongshore-averaged over 90 m ($696 \le y \le 786$ m, Figure 6, solid curves). A simulation with higher spatial resolution (1 m) performed for the same conditions as S1 resulted in similar errors between the modeled and observed wave height and velocities. Errors in H_s are larger than results from 3D simulations with small alongshore bathymetric variability (Rijnsdorp et al., 2015), whereas the absolute biases are similar to 2-layer simulations at Duck, NC (Gomes et al., 2016). The wave breaking parameters, α and β (Appendix A) were set to standard values from the literature and were not tuned to this data set. Although dissipation due to wave breaking may be improved with higher resolution simulations, increasing the number of vertical layers led to instabilities. Due to the bathymetric uncertainty and a focus on understanding circulation dynamics rather than accurate hindcasting, tuning of the vertical resolution to minimize errors between the observed and modeled H_s was not investigated here.

The observed and simulated hour-averaged velocities include strong offshore-directed cross-shore velocities, $\langle u \rangle$, as part of bathymetric rip-current circulation cells, and alongshore velocities, $\langle v \rangle$, that meander around prominent bathymetric features with weaker $\langle v \rangle$ in the center of circulation cells (e.g., $y = 741$ m, Figures 4a and 4c, 5a). The modeled depth-averaged velocities are on average higher than the observed velocities (bias = 0.04 m/s), but almost always are within the alongshore range (Figure 6, shaded regions, comparisons with depth-varying velocities at the instrument elevations are similar). For small shore-normal wave conditions (S1), the modeled and observed velocities have similar magnitudes with small differences that may be owing to localized bathymetric variability not resolved by the surveys or to migration of bathymetric features after the October 14 survey (Figures 6b and 6c). For the moderate-energy shore-normal wave condition (S3a), the strongest modeled $\langle u \rangle$ appear to be shifted in the positive alongshore direction relative to the observations (Figure 5a), which may be due to migration of bathymetric features resulting from strong alongshore currents between October 14 and October 28.

To determine the sensitivity of the H_s and hour-averaged velocity spatial patterns to bathymetric variability, an additional simulation was conducted with bathymetry from November 16 and the moderate-energy shore-normal wave conditions observed on October 28 (S3b, same wave conditions as S3a). October 28 is approximately halfway between the dates of two bathymetry surveys (Figures 1a and 1b). The modeled $S_{\eta\eta}$ at $h = 6$ m is not sensitive to the survey bathymetry, but surfzone H_s are smaller in S3b than in S3a, and thus are more similar to observations (S3a: bias = 0.40 m, S3b: bias = 0.23 m, Figures 5b, 5d and 6d, compare black with red curves). In S3b, the position of the modeled circulation features, including the strong offshore-directed velocities, is similar to that of the observations, leading to smaller errors in a point-to-point comparison (S3a: RMSE = 0.30 m/s, S3b: RMSE = 0.13 m/s, Figures 5a, 5c, 6e and 6f).

3.2. Vorticity Wavenumber Spectra

The cross-shore and vertical variability of eddy length scales on alongshore-variable bathymetry is not known. Here, the alongshore wavenumber spectra of the modeled vertical vorticity is considered for shore-normal waves ($H_s = 2$ m) with different directional spreads (S3a, S4, S5) and alongshore bathymetric variability (S3a, S6, S7, Table 2). The cross-shore coordinate is normalized by the surfzone width, L_{sz}

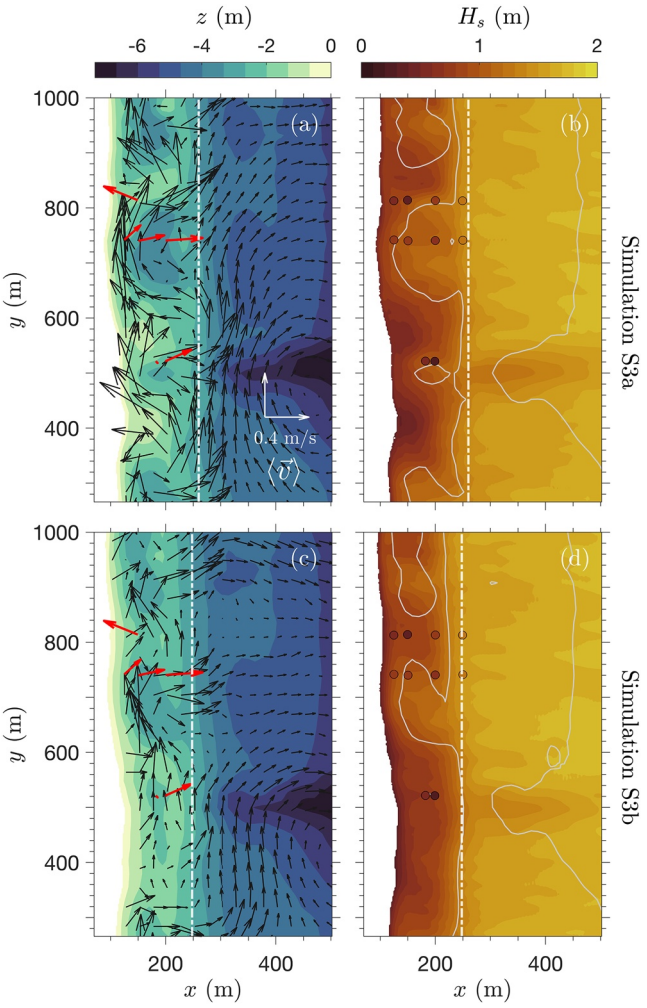

Figure 5. Observed (left: red arrows, right: filled circles) and modeled (left: black arrows, right: color contours) (a and c) hour-averaged depth-averaged velocity, $\langle \vec{v} \rangle$ and (b and d) significant wave height, H_s for moderate-energy shore-normal wave conditions on October 28 with (a and b) October 14 (S3a) and (c and d) November 16 (S3b) bathymetry. Bathymetry (left: color contours, right: gray contour curves at 2.5 and 5.0 m depth) and the approximate outer edge of the surf zone (x_{sz}, all panels: dashed-white lines) are shown. The $\langle \vec{v} \rangle$ scale (left) and H_s colorbar (right) span approximately twice the range of those in Figure 4.

(Table 1), where $L_{sz} = x_{sz} - x_{sl}$, where x_{sz} is the position of the outer edge of the surf zone, and x_{sl} is the alongshore-mean position of the still-water shoreline. Swashzone dynamics, including strong runup and backwash velocities, along an alongshore-varying shoreline may dominate the vorticity field near and in the swash zone ($0L_{sz} < x - x_{sl} < 0.2L_{sz}$) and are not shown here, where the focus is on the inner ($0.2L_{sz} < x - x_{sl} < 0.5L_{sz}$) and outer surf zones ($0.5L_{sz} < x - x_{sl} < 1.0L_{sz}$), and just offshore of the surf zone ($1.0L_{sz} < x - x_{sl} < 1.5L_{sz}$).

3.2.1. Cross-Shore Variability of the Alongshore Wavenumber Spectra of Vorticity

For simulations conducted with observed October 14 bathymetry ($\sigma_{y,sz} = 0.86$ m) and different offshore directional spreads (S3a, S4, and S5), the magnitude of the alongshore wavenumber spectra of depth-averaged vertical vorticity ($S_{\omega\omega}$) is largest at large length scales ($L > 100$ m) and is insensitive to directional spread in the inner surf zone (Figure 7a). In contrast, in the outer surf zone and immediately outside the surf zone, $S_{\omega\omega}$ has more variance at large length scales for simulations with less directional spread (Figures 7b and 7c). The magnitude of $S_{\omega\omega}$ at small length scales ($\mathcal{O}(10)$m), hypothesized to be associated with injection of vorticity from finite-crested breaking waves, is highest for the largest wave directional spread (S3a) at all cross-shore positions (Figure 7, top row). For the simulation with the largest directional spread (S3a, $\sigma_\theta = 28.6°$), the magnitude of $S_{\omega\omega}$ at $L < 85$ m in the outer surf zone, where wave breaking is strong, is larger than the magnitude in the inner surf zone and just offshore of the surf zone (Figure 7, top row, compare solid curves at $L^{-1} > 10^{-2}$ m^{-1}).

For simulations with observed offshore directional spread ($\sigma_\theta = 28.6°$) and differing alongshore bathymetric variability (S3a, S6, S7, Table 2), the variance of vorticity fluctuations at large length scales ($L > 100$ m) increases with increasing alongshore bathymetric variability (Figure 7, bottom row). The largest sensitivity to bathymetry of the $S_{\omega\omega}$ magnitude at large length scales occurred in the inner surf zone (Figure 7d), where deep trough and terrace bathymetric features are present. In contrast, the variance of small length-scale eddies ($\mathcal{O}(10)$ m) is similar and relatively independent of alongshore bathymetric variability (Figures 7d–7f).

3.2.2. Vertical Variability of the Alongshore Wavenumber Spectra of Vorticity

The cross-shore variability of eddy length scales has been investigated with models that account for the generation of eddies from short-crested wave breaking (Kumar & Feddersen, 2017; O'Dea et al., 2021). However, the vertical variability of eddy length scales is not known and has not been investigated using a three-dimensional phase-resolving model. Here, the alongshore wavenumber spectra of vertical vorticity at different elevations ($S_{\omega\omega}(z)$, computed with interpolated horizontal velocities, Section 2.3) are used to investigate the vertical variability of eddy length scales in the surf zone for shore-normal waves with October 14 observed (S3a, Figures 8a–8c) and alongshore-averaged (S7, Figures 8d–8f) bathymetry. The magnitude of $S_{\omega\omega}(z)$ at large length scales ($L > 100$ m) is larger at all depths for the alongshore-varying (S3a) than for the alongshore-uniform (S7) bathymetry (compare Figures 8a–8c with Figures 8d–8f), consistent with the wavenumber spectra computed from the depth-averaged velocities ($S_{\omega\omega}$, Figure 7).

The magnitude of $S_{\omega\omega}(z)$ is nearly depth uniform outside of (not shown) and at the outer edge (Figures 8c and 8f) of the surf zone, and decays slightly with decreasing vertical elevations, primarily for small length-scale eddies, in the outer surf zone in both examples (Figures 8b and 8e) and in the inner surf zone for the

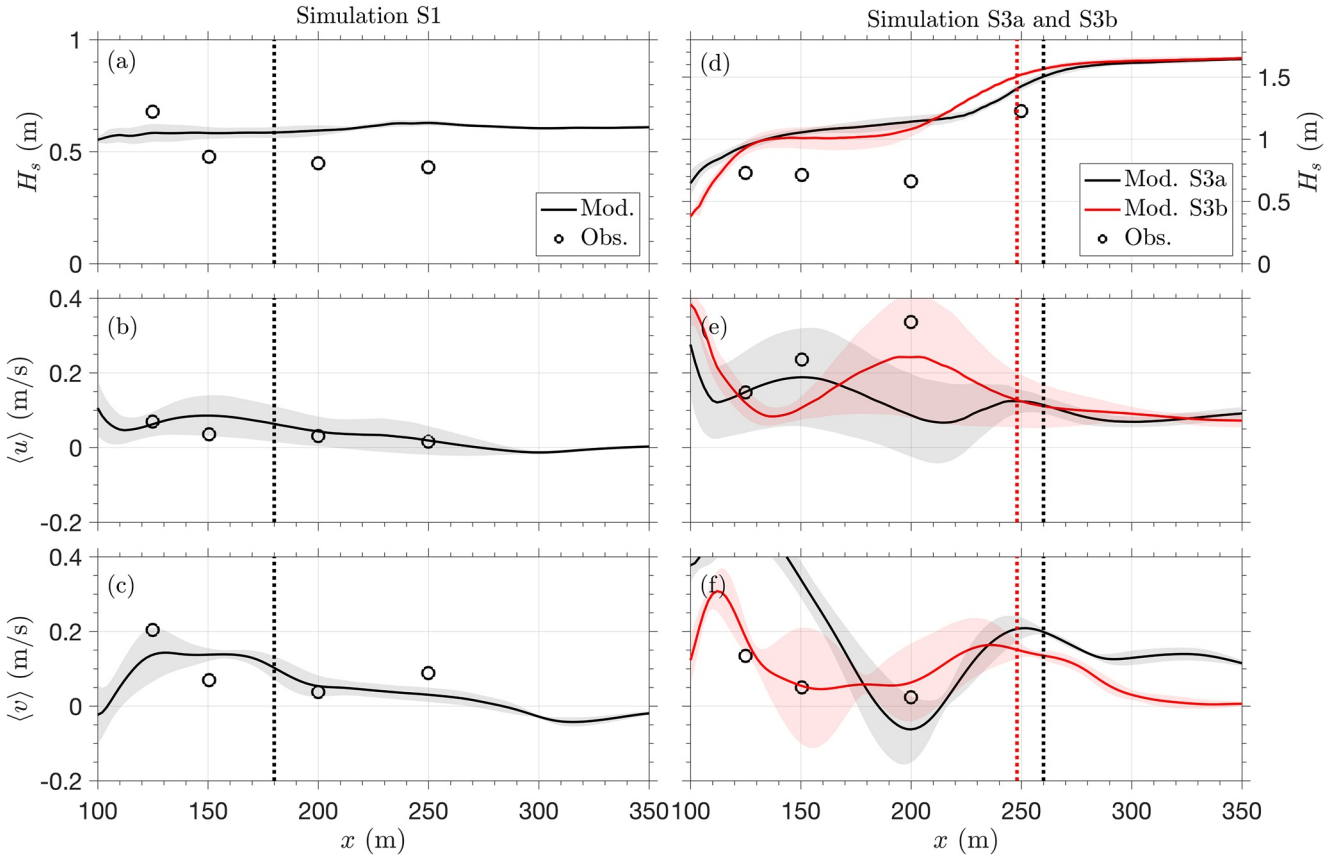

Figure 6. Observed (circles) and modeled (curves) (a and d) significant wave height, H_s and (b and e) 1 h mean cross-shore, $\langle u \rangle$ and (c and f) alongshore $\langle v \rangle$ velocities along the cross-shore transect at $y = 741$ m (Figure 1) for simulations S1 (left), S3a (right, black), and S3b (right, red). Model results are represented as the cross-shore profiles of 90 m alongshore-averaged (curves) and standard deviation (shaded areas) of wave and current statistics. The black (S1, S3a) and red (S3b) dashed vertical lines are the alongshore-averaged outer edge of the surf zone, x_{sz}.

alongshore-uniform bathymetry (Figure 8d). The vertical dependence of $S_{\omega\omega}(z)$ in the inner surf zone for the alongshore-variable bathymetry is not evaluated here due to the inability to resolve $S_{\omega\omega}(z)$ at elevations that are below the seafloor at some alongshore locations (e.g., $z < -0.75$ m at $0.5L_{sz}$, Figure 8a). For the alongshore-variable bathymetry simulation (S3a), the vorticity variance (the area under $S_{\omega\omega}(z)$) for small eddy length scales ($L < 100$ m) decays by 36% over 1 m in the water column in the outer surf zone (Figure 8b), whereas the vorticity variance for small length scales decreases by less than 15% over 2 m in the water column at the outer edge of the surf zone (Figure 8c). In the inner and outer surf zone for the alongshore-uniform bathymetry simulation (S7), the vorticity variance from near the surface ($z = -0.25$ m) to the lowest resolved elevation in the water column decays by ≥ 45% for small eddy length scales and >25% for large eddy length scales (Figures 8d and 8e).

Furthermore, the mean eddy length scale, $\bar{L}$ ($= \bar{k}_y / 2\pi$, energy-weighted average length scale, the centroid of the spectrum, Figure 8, circles) of $S_{\omega\omega}(z)$ increases with decreasing vertical elevations in the surf zone for nearly all simulations (wavenumber decreases with decreasing vertical elevations, Figures 8b, 8d and 8e) and decreases or remains approximately the same over the vertical near the surfzone edge (Figures 8c and 8f) and just offshore of the surf zone (not shown). For the simulation with the observed bathymetry (S3a), $\bar{L}$ near-surface is ~46 m and increases to ~53 m over 1.25 m in the water column in the outer surf zone (Figure 8b). Similarly, for the alongshore-uniform bathymetry simulation (S7), $\bar{L}$ is ~39 m near the surface and increases to ~45 m over 1.5 m in the water column in the inner surf zone (Figure 8d).

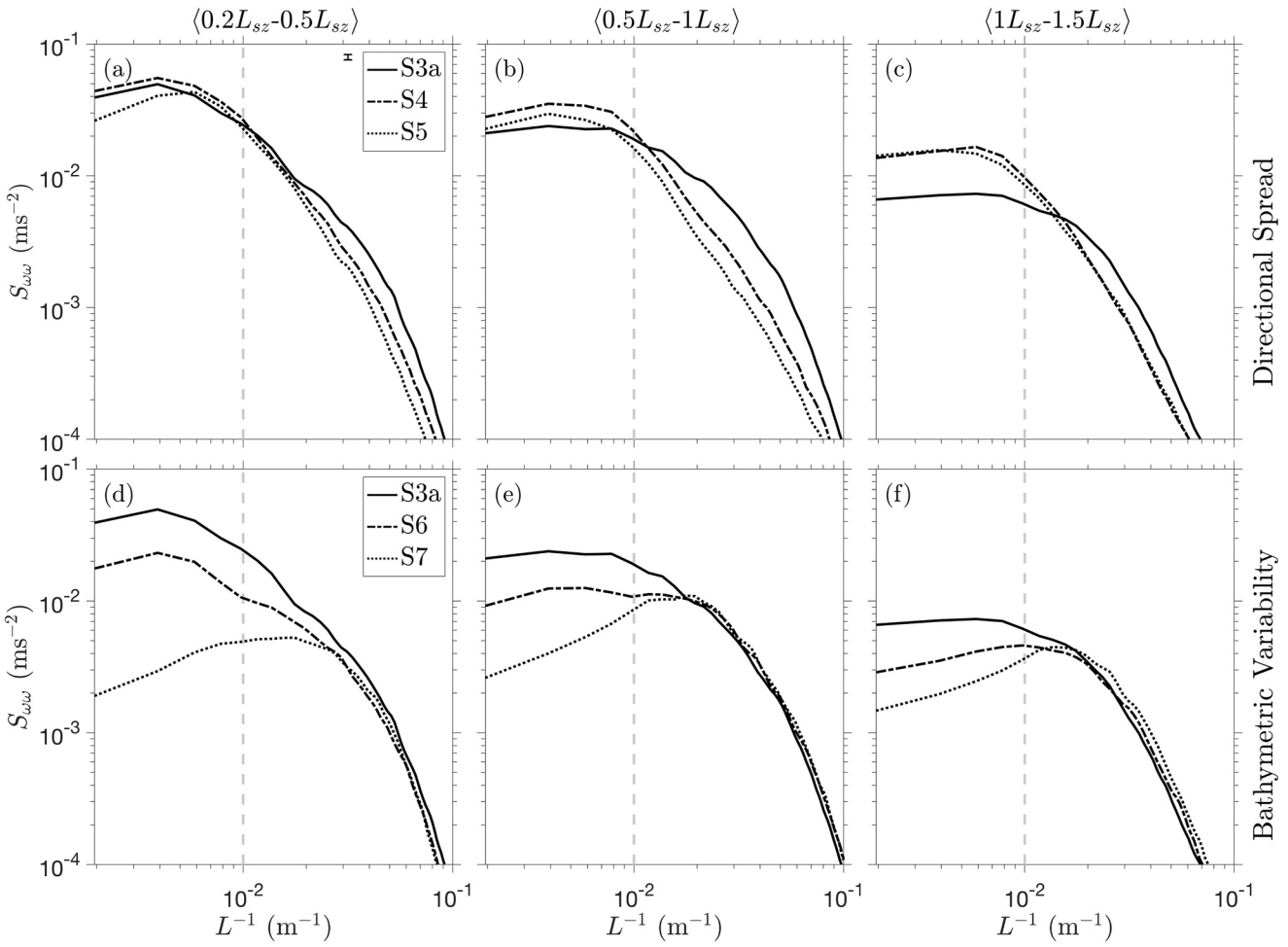

Figure 7. Cross-shore average of the alongshore wavenumber spectra of vorticity ($S_{\omega\omega}$) versus the inverse alongshore length scale (wavenumber divided by 2π, $L^{-1} = k_y/2\pi$, vertical dashed gray lines at $L = 100$ m) for (a) and (d) the inner surf zone ($0.2L_{sz} < x - x_{sl} < 0.5L_{sz}$), (b) and (e) the outer surf zone ($0.5L_{sz} < x - x_{sl} < 1.0L_{sz}$), and (c and f) just offshore of the surf zone edge ($1.0L_{sz} < x - x_{sl} < 1.5L_{sz}$) for (a)–(c) simulations with observed bathymetry and forced with large directional spread (S3a, $\sigma_\theta = 28.6°$, solid curves), half the directional spread (S4, $\sigma_\theta = 14.3°$, dot-dashed curves), and no directional spread (S5, $\sigma_\theta = 0°$, dotted curves), and for (d)–(f) simulations with directionally spread waves ($\sigma_\theta = 28.6°$) and observed Oct. 15 bathymetry (S3a, $\sigma_{y,sz} = 0.86$ m, solid curves), half the observed alongshore bathymetric variability (S6, $\sigma_{y,sz} = 0.43$ m, dot-dashed curves), and alongshore-averaged bathymetry (S7, $\sigma_{y,sz} = 0$ m, dotted curves). The vertical bar in (a) indicates the 95% confidence interval for 3540 DOF.

3.3. Vertical Structure of Very Low-Frequency Motion

Field observations suggest there may be vertically varying structure of low-frequency eddies in the outer surf zone, but less variation in shallower depths (Lippmann et al., 2016; Henderson et al., 2017). Here, the very low-frequency (VLF, $0.003 < f < 0.007$, Section 2.3, Figure 2) velocities from the simulation with moderate-energy shore-normal waves and Oct. 14 observed bathymetry (S3a, Figure 1) vary along the barred cross-shore profile ($y = 741$ m) and vertically in the outer surf zone (Figure 9). In the outer surf zone, the change in simulated cross-shore (alongshore) VLF velocities are up to 0.14 m/s (0.12 m/s) over the water column (not shown). The VLF velocity spectral density varies in the cross-shore, with the highest cross-shore VLF spectral density near the bar crest at $x = 220$–240 m (Figure 9a) and the highest alongshore VLF spectral density near the shoreline at $x < 100$ m (Figure 9e). The cross- and alongshore spectral densities are similar in magnitude at all locations, except near the bar crest where the cross-shore spectral density is much greater than the alongshore spectral density (Figures 9a and 9e). The coherence of VLF velocities at different elevations in the water column with those near the surface decreases with distance below the surface, including near the wave breaking region (around the bar crest, $x = 200$–270 m, Figures 9b and 9f). The VLF phase relative to the phase at the surface changes sign in the cross-shore (Figures 9c and 9g), indicating

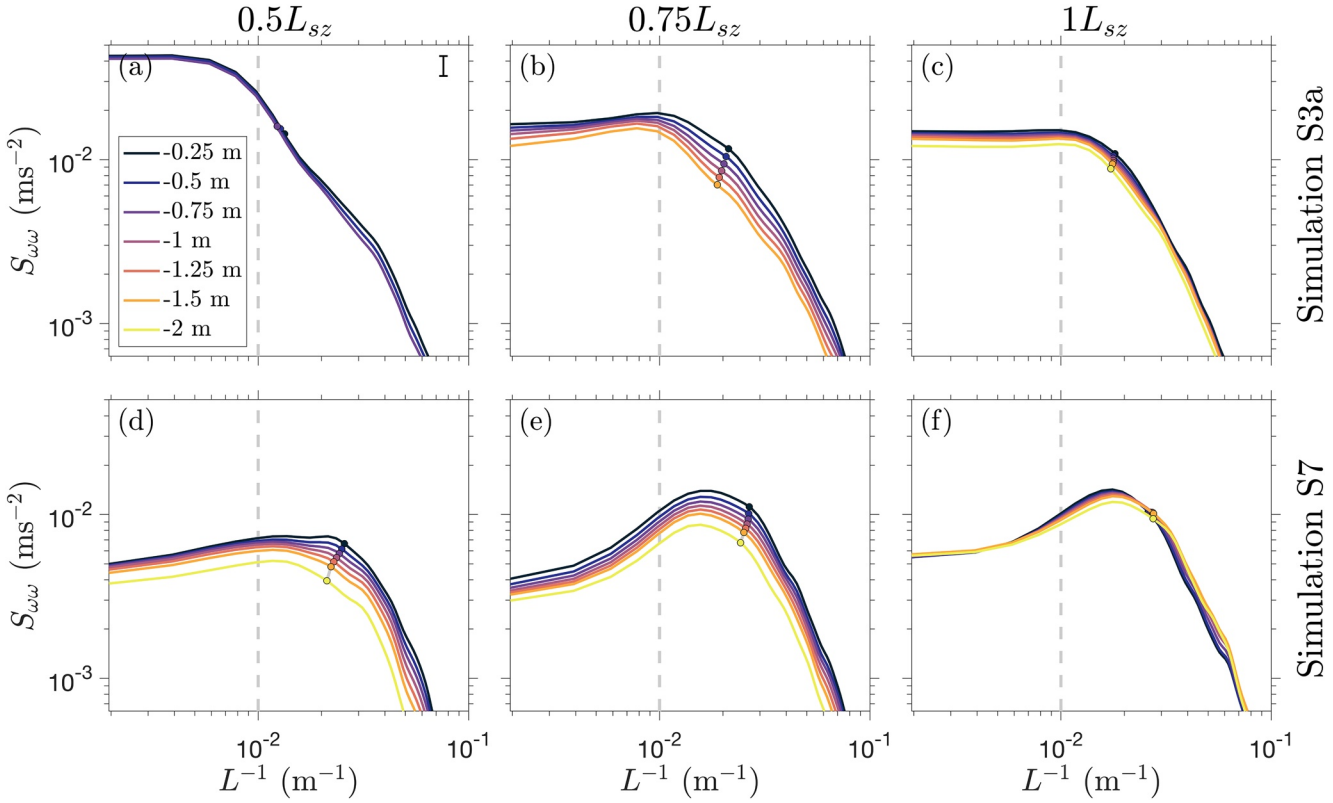

Figure 8. The alongshore wavenumber spectral density of vorticity ($S_{\omega\omega}(z)$) versus the inverse alongshore length scale (wavenumber divided by 2π, $L^{-1} = k_y/2\pi$, vertical dashed gray line at $L = 100$ m) for normalized cross-shore positions (a) and (d) in the inner surf zone ($x - x_{sl} = 0.5L_{sz}$), (b and e) the outer surf zone ($x - x_{sl} = 0.75L_{sz}$) and (c and f) the outer edge of the surf zone ($x - x_{sl} = 1.0L_{sz}$). At each location, the colored curves (legend inset, lighter curves nearer to the seafloor) are the spectra at 0.25–2 m below the mean sea-surface elevation for (a)–(c) observed bathymetry (S3a) and (d)–(f) alongshore-uniform bathymetry (S7). The circles (colored by elevation) are at the mean eddy length scale, $\overline{L}$ (centroid). The vertical bar (a) indicates the 95% confidence interval for 354 DOF.

that near-bottom velocities alternate between leading and lagging surface velocities. The root-mean-squared (rms) VLF cross-shore velocities decrease with depth in the trough and near the bar crest ($x = 175$–190 and $x = 220$–240 m, Figure 9d), indicating more variable VLF velocities near the surface onshore of the onset of wave breaking. The rms VLF alongshore velocities have relatively small vertical dependence onshore and offshore of the bar (Figure 9h).

Cross-shore transects at other regions of the S3a domain (e.g., the terraced beach profile at $y \approx 850$ m, Figure 1) have similar vertical dependence in the outer surf zone (e.g., $0.75L_{sz}$), as do VLF velocities with alongshore-uniform bathymetry (S7 simulation, not shown), suggesting that there is vertical variation of VLF velocities in the outer surf zone, with decreasing vertical dependence toward the shore for both the simulated alongshore-uniform and alongshore-varying bathymetry.

4. Discussion

4.1. Cross-Shore Variability of Vorticity Wavenumber Spectra

The length scales of horizontal eddies and their dependence on the incident wave forcing, coupled with the role of surfzone bathymetry, is a focus of recent studies (Feddersen, 2014; Kumar & Feddersen, 2017; O'Dea et al., 2021). Here, for simulations with varying offshore directional spread (σ_θ) on an alongshore inhomogeneous bathymetry, the vorticity variance, $\sigma^2_{\omega\omega}$ (the area under alongshore wavenumber spectra of depth-averaged vertical vorticity separated for inverse length scales (wavenumbers divided by 2π, $L^{-1} = k_y/2\pi$) on either side of 0.01 m^{-1}, $S_{\omega\omega}$, in Figure 7) at small length scales ($L < 100$ m) increases with directional spread in all cross-shore regions (Figure 10a, circles, squares, triangles, and linear fit with slopes = 3.2, 6.0, and 0.6×10^{-6} m^{-1}s^{-2}, respectively), consistent with results from previous modeling studies using a

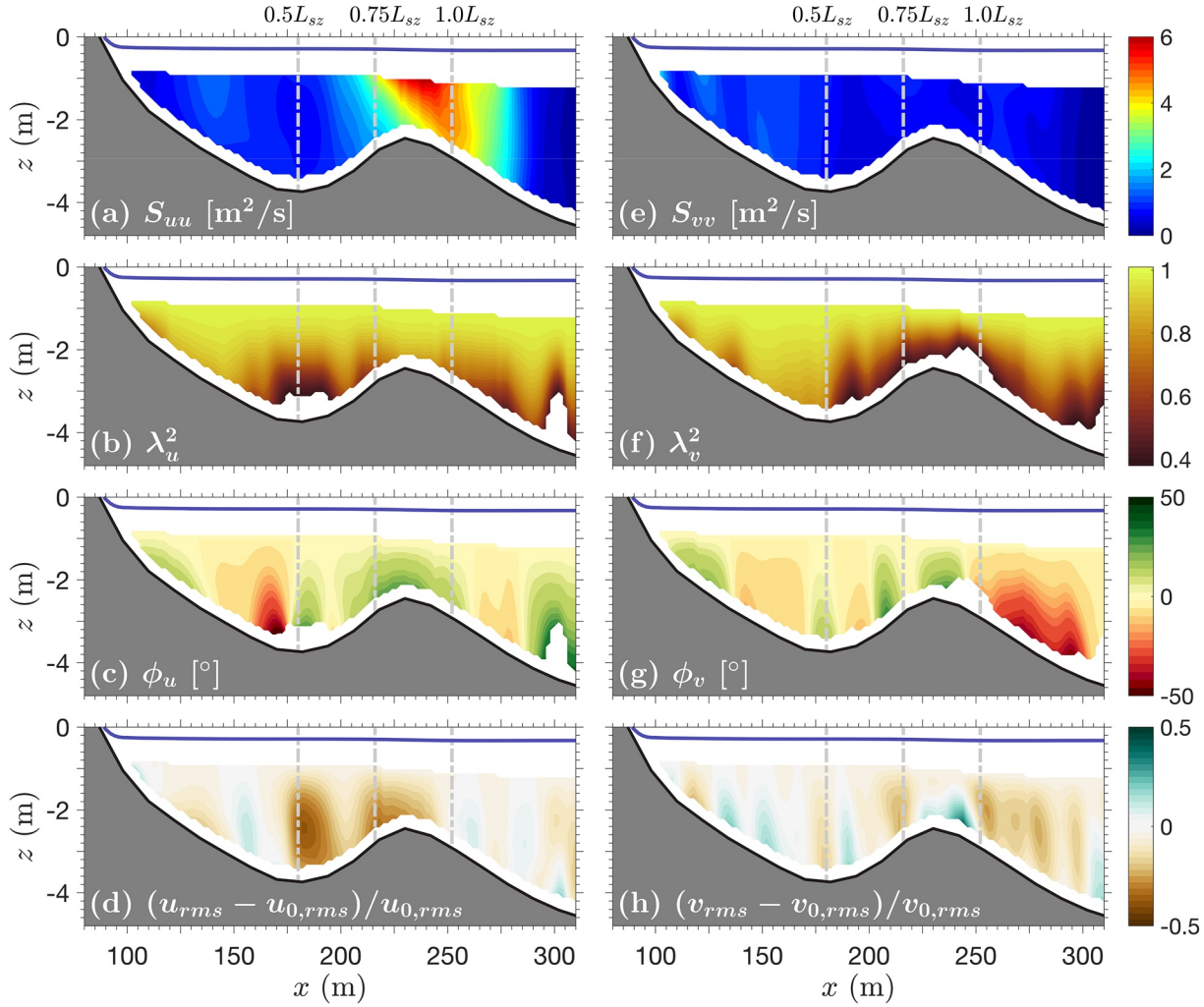

Figure 9. Cross-shore transect for the simulation S3a at y = 741 m of the (a)–(d) cross- and (e)–(h) alongshore VLF velocity spectral density (a: S_{uu}, e: S_{vv}), squared coherence (b: λ_u^2, f: λ_v^2), phase shift (c: ϕ_u, g: ϕ_v), and the normalized root-mean-squared (rms) difference (d: $(u_{rms} - u_{0,rms})/u_{0,rms}$, h: $(v_{rms} - v_{0,rms})/v_{0,rms}$) where negative (positive) indicates less (more) variability compared with the surface, with the mean sea-surface elevation (blue) and surfzone regions (dashed gray lines). Values are not shown for coherence squared and phase when the coherence is less than the 95% significance level.

depth-integrated wave-resolving Boussinesq model with alongshore-uniform bathymetry (Spydell & Feddersen, 2009; Suanda & Feddersen, 2015) and alongshore-variable bathymetry (O'Dea et al., 2021). Multiple surfzone processes may contribute to the vorticity variance at small length scales, including generation by directionally spread short-crested breaking waves (e.g., σ_θ = 28.6° in S3a). The small length-scale ($\mathcal{O}$(10) m) vorticity injected during wave breaking may be transferred to longer length scales through an inverse cascade (Boffetta & Ecke, 2012; Bühler & Jacobson, 2001; Elgar et al., 2019; Elgar & Raubenheimer, 2020; Feddersen, 2014) or dissipated through bottom friction.

In contrast to small length scales, the dependence of large length-scale (L > 100 m) vorticity variance on directional spread differs by region within the surf zone, possibly owing to eddy coalescence and pulsations in mean circulation patterns. In the inner surf zone, vorticity variance at large length scales are small and weakly increase with directional spread (Figure 10b, circles and linear fit with slope = 1.3×10^{-6} m^{-1}s^{-2}), possibly as a result of the enhancement of the coalescence of small length-scale eddies generated by short-crested wave breaking in the highly variable inner surf zone (Bühler & Jacobson, 2001; Clark et al., 2012; Spydell & Feddersen, 2009) or fluctuations of strong inner surf zone circulation patterns (Figure 5a). In contrast, in the outer surf zone and just offshore of the surf zone, the vorticity variance at large length scales decreases with directional spread (Figure 10b, squares, triangles, and linear fit with slope = -0.6 and -2.2×10^{-6} m^{-1}s^{-2},

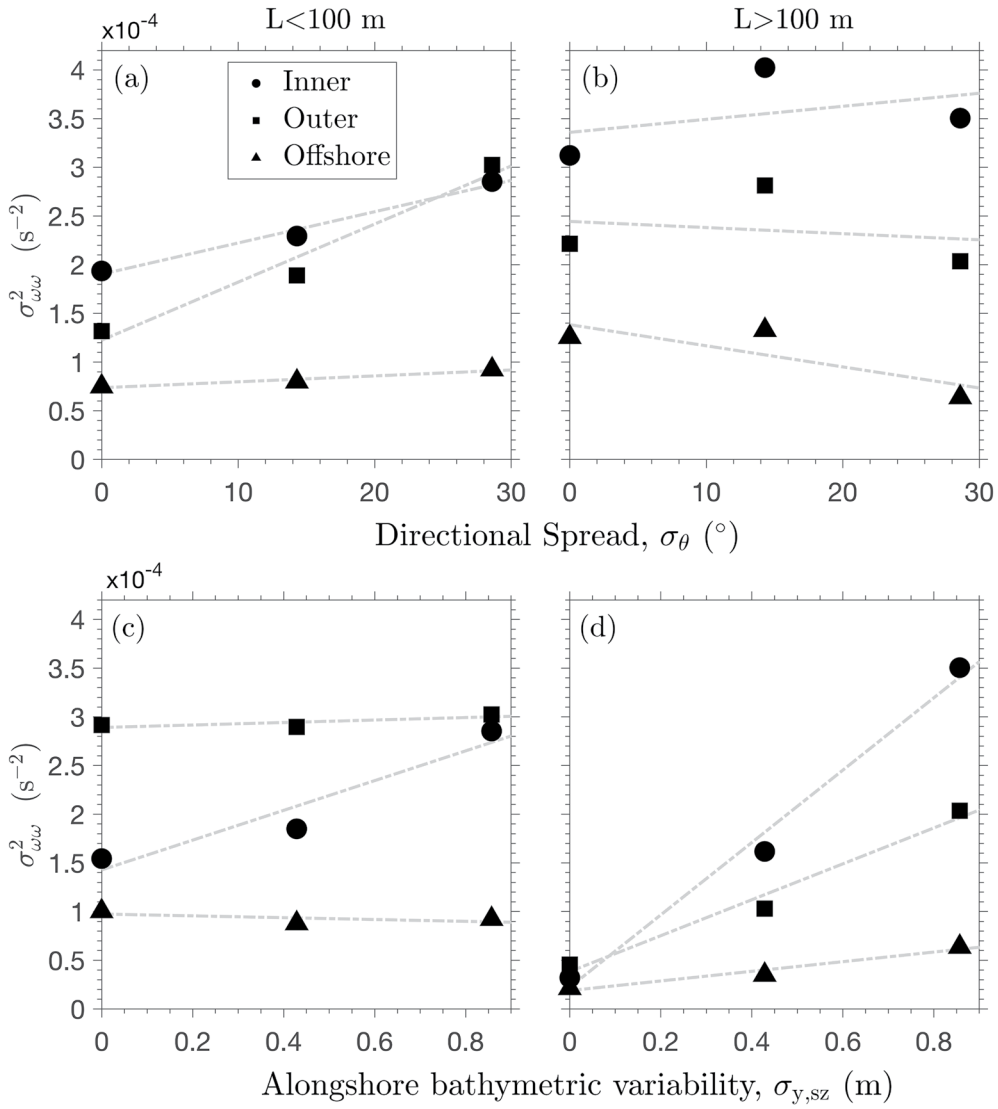

Figure 10. Vorticity variance, $\sigma^2_{\omega\omega}$ versus (a and b) directional spread, σ_θ (S3a, S4, and S5) and (c and d) the standard deviation of surfzone bathymetric variability, $\sigma_{y,sz}$ (S3a, S6, and S7) for (a and c) small ($L < 100$ m) and (b and d) large ($L > 100$ m) eddy length scales for the inner (circles, $0.2L_{sz} < x - x_{sl} < 0.5L_{sz}$), outer (squares, $0.5L_{sz} < x - x_{sl} < 1.0L_{sz}$), and offshore (triangles, $1.0L_{sz} < x - x_{sl} < 1.5L_{sz}$) of the surf zone. Linear least squares fits are given by the dashed-gray lines.

respectively), which may result from fluctuations of strong mean circulation features that extend farther offshore for simulations with variable bathymetry and less directional spread (O'Dea et al., 2021). Previous funwaveC simulations with alongshore-uniform bathymetry found that the variance at all length scales increased considerably with directional spread in the inner surf zone (Spydell & Feddersen, 2009), whereas for SWASH simulations with alongshore-variable bathymetry, the vorticity variance in the inner surf zone increased significantly with directional spread at small length scales and only weakly increased with directional spread at large length scales (Figures 10a and 10b).

For simulations with a range of alongshore bathymetric variability (the maximum alongshore standard deviation of the seafloor elevation, $\sigma_{y,sz}$), the vorticity variance at small length scales ($L < 100$ m) is independent of bathymetric variability in the outer surf zone and just offshore of the surf zone (Figure 10c, triangles, squares, and linear fits with slopes $= -0.2$ and -0.1×10^{-4} m^{-1}s^{-2}, respectively), suggesting that small length-scale eddy generation is primarily a function of the incident wave field, rather than the surfzone

bathymetric variability. However, in the inner surf zone, higher variance of medium length-scale (L = 80–100 m) eddies is present in the simulation with observed bathymetry ($\sigma_{y,sz}$ = 0.86 m) than in simulations with less alongshore variability (Figures 7d and 10c). The source of this additional variance is unknown, but may be related to instabilities of the mean circulation, which tend to have moderate to long length scales associated with the bathymetric variability (Akkermans et al., 2008; Geiman & Kirby, 2013; Tabeling et al., 1990).

In contrast to the vorticity variance at small length scales, which is not strongly dependent on bathymetry, the eddy variance at large length scales (L > 100 m) increases with alongshore bathymetric variability in all regions, particularly in the inner surf zone (Figure 10d, circles and linear fit with slope = 5.0×10^{-4} $m^{-1}s^{-2}$). There is a weaker increase in eddy variance with bathymetric variability in the outer surf zone and offshore of the surf zone (Figure 10d, squares, triangles, and linear fit with slopes = 2.5 and 0.7×10^{-4} $m^{-1}s^{-2}$, respectively). The role of bathymetric variability in controlling surf zone vorticity at large spatial scales, shown here as a function of the cross-shore position in the surf zone and degree of alongshore bathymetric variability, is consistent with previous findings that compared the average variance across the entire surf zone for alongshore-uniform and alongshore-variable bathymetry (O'Dea et al., 2021). Additionally, the vorticity variance at small and large length scales for alongshore-uniform bathymetry (S7) is greatest in the outer surf zone (Figures 10c and 10d), in agreement with previous phase-resolved, depth-averaged model results that found a maximum bulk VLF rotational velocity in the outer surf zone for large, directionally spread waves on alongshore-uniform bathymetry (Feddersen et al., 2011).

The correlation of large-scale eddies with alongshore bathymetric variability, in contrast to no correlation with directional spread, suggests that bathymetric variability influences large-scale low-frequency fluctuations in the surf zone, possibly owing to enhanced eddy interaction and coalescence in depressions or troughs (Figure 1a) (Bühler & Jacobson, 2001). In addition, the highly variable observed bathymetry modulates wave breaking patterns, driving meandering mean currents (Figure 5a), which may pulsate at low frequencies and may shed large eddies (MacMahan et al., 2004; Reniers et al., 2007). Eddy kinetic energy is intensified in the surf zone in simulations with bathymetric variability (O'Dea et al., 2021; Uchiyama et al., 2017). Elevated eddy kinetic energy also is present outside of the surf zone, where oscillations in bathymetrically driven circulation patterns (e.g., rip current jets, Smith & Largier, 1995; Haller & Dalrymple, 2001) or ejections of surfzone eddies (Feddersen, 2014) may result in higher variance at large eddy length scales.

4.2. Vertical Variability of the Vorticity Wavenumber Spectra

Although previous studies have quantified surfzone eddy variability with alongshore arrays of electromagnetic current meters at one elevation in the water column (Noyes et al., 2004; Oltman-Shay et al., 1989), the depth variability of eddies in the surf zone has been investigated in only a few studies, and no previous numerical modeling experiments have investigated the vertical variability of vortical motion with a fully three-dimensional phase-resolving model. Simulations with phase-averaged models have shown vertical structure of shear instabilities (Newberger & Allen, 2007a, 2007b) and the effect of vortex tilting on the surf zone vorticity budget (Uchiyama et al., 2017). However, these models do not include wave-forced eddy generation, which is an important source of eddy energy and may influence the vertical structure of eddies (Newberger & Allen, 2007a).

Here, the energy levels of the alongshore wavenumber spectra of the simulated vertical vorticity ($S_{\omega\omega}(z)$) decrease slightly from the surface to the seafloor, particularly for small length-scale eddies, and the mean eddy length scales (centroids of the spectra) increase (Figure 8, circles) in some locations in the nearshore for all simulations, indicating that eddies may exhibit elevation dependence for beaches with uniform or alongshore-varying bathymetry. The change in magnitude and mean length scale of $S_{\omega\omega}(z)$ with elevation within the water column may be related to length-scale dependent attenuation and the combined effects of bottom boundary layer dynamics, vertical mixing, and the vertical distribution of shear instabilities (Lippmann & Bowen, 2016), which could result in depth variation of eddy stretching and tilting, as seen in three-dimensional phase-averaged ROMS simulations (Uchiyama et al., 2017). The vertical dependence of $S_{\omega\omega}(z)$ may be sensitive to changes in the vertical eddy viscosity (Lippmann & Bowen, 2016) and the incorporation of wave breaking related turbulence production (Feddersen & Trowbridge, 2005).

Simulations with alongshore-uniform bathymetry exhibit vertical variation at all length scales, whereas simulations with alongshore-variable bathymetry only have vertical variation in the outer surf zone (compare Figures 8a–8c with Figures 8d–8f), indicating that bathymetric variability may play a role in reducing the vertical dependence of large length-scale eddies. Although there is some vertical variation of eddies at all length-scales on alongshore-uniform beaches (Figures 8d and 8e), on beaches with alongshore-varying bathymetry the vertical dependence at small length scales decreases somewhat in the outer surf zone (Figure 8b) and is negligible in the inner and outer edge of the surf zone (Figures 8a and 8c). Thus, whereas small length-scale eddies may exhibit vertical dependence in the outer surf zone on beaches with large alongshore variability, larger length-scale eddies may be nearly depth-uniform on alongshore-variable bathymetry.

4.3. Vertical Structure of Very Low-Frequency Motion

The three-dimensionality of VLF currents, which may impact material exchange and dispersion, is not well documented. Similar to the small number of observations of VLF motion vertical structure (Henderson et al., 2017; Lippmann et al., 2016), VLF motion simulated with SWASH varies in the vertical near the bar crest (Figure 9). Cross-shore energy density decays with depth, with over an 60% drop in squared coherence over the water column, and with large phase shifts near the bottom (up to 50°) relative to near-surface velocities (Lippmann et al., 2016). Simulated VLF velocities have weak vertical dependence of VLF motions near the outer edge of the surf zone with little vertical variation in shallower depths, broadly consistent with observations (Henderson et al., 2017; Lippmann et al., 2016).

Here, the simulated VLF motion exhibits vertical dependence in the outer surf zone, (e.g., immediately onshore of the bar crest, $0.75L_{sz}$, Figures 8b and 9), with decreasing vertical dependence toward the inner surf zone. Furthermore, simulated VLF velocities are elevation dependent for the terraced profile of S3a at $y \approx 850$ m (not shown), and for alongshore-uniform bathymetry (S7, not shown). A theoretical model for eddy vertical dependence for a scenario with a depth-uniform alongshore mean current, constant eddy viscosity, no incorporation of surface sheer stresses from wave breaking, and varying bottom friction (Lippmann & Bowen, 2016) suggests the vertical structure of eddies in the surf zone may result from instabilities and bottom boundary layer dynamics. These solutions, which include bottom friction and linearized lateral momentum advection, suggest that eddy vertical structure may depend on vertical mixing, eddy scales, and the magnitude of shear in a mean alongshore current, but do not address shear in the cross-shore current or the role of variability in wave forcing in a phase-resolved framework.

The analyses here build on previous studies to investigate surfzone eddy dynamics by examining the alongshore length scales at lower frequencies than surface gravity waves (O'Dea et al., 2021; Spydell & Feddersen, 2009) and cross-shore profiles of VLF flows ($0.003 < f < 0.007$ Hz) (Henderson et al., 2017; Lippmann et al., 2016). The vertical dependence of $S_{\omega\omega}(z)$ and VLF horizontal velocities is largest in the outer surf zone ($0.75L_{sz}$, Figures 8b and 8e, 9), and decreases toward the shoreline. Near $0.5L_{sz}$, the coherence with near-surface cross-shore flows decreases toward the seafloor (Figure 9b), whereas it was not possible to fully assess the vertical dependence of the alongshore eddy length scales at $0.5L_{sz}$ for the alongshore-variable bathymetry because the varying water depths preclude computing $S_{\omega\omega}(k)$ for $z < 0.75$ m. The vertical dependence of $S_{\omega\omega}(k)$ and VLF velocities may be influenced by vertical eddy viscosity, bottom drag, and absence of breaking-wave-generated turbulence in SWASH simulations. Although simulations suggest that low-frequency motions are primarily two-dimensional with some vertical structure, additional observational and numerical studies are necessary to understand the complex three-dimensional structure of VLF velocities in the surf zone, including the sensitivity of VLF velocities to wave conditions and surf zone bathymetries, and the implications for cross-shore exchange.

5. Conclusions

Simulations with a three-dimensional phase-resolving model (SWASH) reproduce the observed trends in wave transformation and the spatial patterns and magnitudes of the mean alongshore currents and meandering circulation on a barred beach with alongshore-inhomogeneous bathymetry. However, circulation features were sometimes shifted spatially relative to the observations, and the simulated significant wave

height was overestimated in the surf zone. The simulated surf zone circulation was sensitive to the bathymetry, which evolved during the field study.

The modeled dynamics include the horizontal and vertically dependent structure of vortical motion in the surf zone. The alongshore eddy length scales were quantified using the alongshore wavenumber spectra of depth-averaged vorticity for simulations with different wave directional spreads and alongshore bathymetric variability. The variance of small length-scale eddies ($\mathcal{O}(10)$ m) increases with directional spread and is independent of alongshore bathymetric variability in the outer surf zone and just offshore of the surf zone, suggesting that vortical motion with short alongshore length scales may be related to the incident wave field, and in particular to forcing by short-crested wave breaking, consistent with previous findings (Spydell & Feddersen, 2009; Suanda & Feddersen, 2015). The variance of large length-scale eddies ($\mathcal{O}(100)$ m) increases with alongshore bathymetric variability, indicating that alongshore bathymetric variability may intensify the formation of large length-scale eddies, in agreement with Bousinessq simulations with variability bathymetry (O'Dea et al., 2021). The variance of large length-scale eddies decreases with increasing directional spread in the outer surf zone and just offshore of the surf zone, suggesting that the relationship between directional spread and large length-scale eddies is not well understood, but may be related to instabilities in the stronger mean circulation in cases with less directional spread.

Modeled eddy length scales and low-frequency horizontal velocities were primarily two-dimensional with weak dependence on elevation in the outer surf zone, and occasionally in the inner surf zone for both alongshore-uniform and alongshore-variable bathymetry. The magnitude of the alongshore wavenumber spectra of vorticity decreased, specifically at small length scales, and the mean length scale (spectral centroid) increased between the surface and the seafloor within the surf zone, whereas the vertical variation at the edge of the surf zone and just outside of the surf zone was small. The horizontal and vertical structures of very low-frequency (VLF) motions have complex patterns, including large drops in coherence and changes in phase between near-surface and subsurface flows. The vertical dependence of VLF velocities decreases from the outer surf zone toward the shoreline, broadly consistent with previous field studies (Henderson et al., 2017; Lippmann et al., 2016). Further investigation is necessary to understand the complex three-dimensional vertical and horizontal variability of low-frequency motions in the surf zone.

Appendix A: Model Description

Simulating WAves till SHore (SWASH) is based on an explicit, second-order finite difference method for horizontally staggered grids, and conserves mass and momentum at discrete levels for an incompressible fluid with a constant density, which enables an efficient scheme to simulate individual wave propagation and breaking with high spatio-temporal resolution (Zijlema & Stelling, 2005; Zijlema et al., 2011). The momentum equations are

$$\frac{\partial u_i}{\partial t} + \frac{\partial u_i u_j}{\partial x_j} = -\frac{1}{\rho}\frac{\partial p_h + p_{nh}}{\partial x_i} + \frac{\partial \tau_{ij}}{\partial x_j} - g\delta_{i3} \tag{A1}$$

and

$$\frac{\partial u_j}{\partial x_j} = 0 \tag{A2}$$

where x and u are the position and velocity in a Cartesian coordinate system ($i, j = 1, 2, 3$). Here, t is time, ρ is density, g is gravitational acceleration, τ_{ij} are turbulent stresses, and p_h (p_{nh}) is hydrostatic, $\rho g z$ (non-hydrostatic, $\rho g\,(\eta - z)$) pressure components. The time evolution of the surface elevation is determined by continuity,

$$\frac{\partial \eta}{\partial t} + \frac{\partial}{\partial x_i}\int_{-h}^{\eta} u_i dz = 0 \tag{A3}$$

where h is the stationary bottom boundary, η is the moving free-surface, and z is the vertical coordinate ($x_{i=3}$). The surface and bottom kinematic boundary layers constrain particle motion, providing the constraints at the fixed bottom,

$$w\big|_{z=-h} = -u_i \frac{\partial h}{\partial x_i} \tag{A4}$$

and the free-surface,

$$w\big|_{z=\eta} = \frac{\partial \eta}{\partial t} + u_i \frac{\partial \eta}{\partial x_i} \tag{A5}$$

where w is the vertical velocity ($u_{i=3}$) and there is a constant pressure ($p_h = p_{nh} = 0$) and no surface stresses at the free-surface. The bottom boundary shear stress, τ_b is based on a quadratic friction law, with the drag coefficient, c_f determined from the Manning-Strickler formulation such that

$$c_f = 0.015(k \,/\, h)^{1/3} \tag{A6}$$

where k is the Nikuradse roughness height, set as 1 mm, within the range of values used in previous studies at this cite (Hsu et al., 2006).

The turbulent stresses are obtained from a turbulent viscosity approximation ($\tau_{xx} = \upsilon_h \frac{\partial u}{\partial x}$, where υ_h is the horizontal eddy viscosity and $\tau_{xz} = \upsilon_v \frac{\partial u}{\partial z}$, where υ_v is the vertical eddy viscosity) (Rijnsdorp et al., 2017; Smit et al., 2013). The horizontal eddy viscosity is approximated with the Smagorinksy model with a Smagorinsky constant of 0.1 (Smagorinsky, 1963), and vertical mixing is approximated using the k–ϵ model, with k the turbulent kinetic energy per unit mass and ϵ the dissipation rate of turbulent kinetic energy per unit mass (Launder & Spalding, 1983). The vertical eddy viscosity allows for diffusion of this stress into the water column, including coupling between vertical layers, and also increases numerical stability (Smit et al., 2013). A 10^{-3} m^2/s background eddy viscosity was specified to account for unresolved vertical mixing, enhancing stability in the model. This value is small compared with the vertical viscosity computed by the standard k–ϵ model. Although the breaking-induced turbulence is not directly implemented in SWASH, model simulations have shown that the turbulent kinetic energy below spilling breakers is well predicted (Rijnsdorp et al., 2017).

The simulation stability was improved further by discretization with flux-limited (shock-resolving) vertical advective terms indicated with the first-order upwind scheme. At points where velocity is computed, the water depths are approximated with the Monotonic Upstream-centered Scheme for Conservation Laws limiter (MUSCL), a finite volume method that improves numerical accuracy. Non-hydrostatic pressure gradients in the vertical momentum equations are approximated with the Keller-box scheme (Lam & Simpson, 1976). Explicit time integration is performed using a specified Courant number between 0.05 and 0.30, and the vertical time integration uses the implicit Euler Scheme.

SWASH simulates wave breaking using a hydrostatic front approximation, similar to disabling dispersive terms in the Boussinesq equations (Tissier et al., 2012; Tonelli & Petti, 2010), by prescribing a hydrostatic pressure distribution in the model around the discontinuity of a breaking wave. The turbulent wave front is regarded as a sub-grid flow feature where the vertical accelerations are not resolved and the non-hydrostatic pressure is set to zero. The hydrostatic front approximation is initiated when local surface steepness exceeds a fraction of the shallow water celerity,

$$\frac{\partial \eta}{\partial x} > \alpha\sqrt{gh} \tag{A7}$$

where α is a parameterized value. The spatial persistence of wave breaking is achieved by labeling a meshpoint for hydrostatic computation if the neighboring grid point has been labeled for hydrostatic computation

and the local steepness exceeds a fraction of the shallow water celerity (Equation 8) where the parameterized value is replaced with a coefficient β. In all simulations, wave breaking is controlled with a threshold parameter for initiation of wave breaking at a mesh-point, $\alpha = 0.6$ (Lynett Patrick, 2006) and for the neighboring mesh-points, $\beta = 0.3$. This approach, combined with the conservation of momentum, leads to appropriate levels of energy dissipation on the front face of a breaking wave (Peregrine, 1983).

Data Availability Statement

Nearshore ADV data used in this study are available at https://doi.org/10.5281/zenodo.4924900 and bathymetry, water levels, and offshore wave data are provided by the USACE at https://frfdataportal.erdc.dren.mil/. Model configuration files, MATLAB processing codes, and model output used to produce figures in this paper are available at https://doi.org/10.5281/zenodo.4141219.

Acknowledgments
The authors thank the staff of the USACE Field Research Facility, Duck, NC, and of the PVLAB at the Woods Hole Oceanographic Institution for helping deploy, maintain, and recover sensors, for providing data from long-term sensors, and for bathymetric surveys. Also, the authors thank Pieter Smit for assistance with the model setup, and Jim Thomson, Falk Fedderson, and other reviewers for useful comments on the manuscript. Support was provided by the University of Washington Royalty Research Fund, the National Science Foundation, the Office of Naval Research, a National Defense Science and Engineering Graduate Fellowship, a Vannevar Bush Faculty Fellowship, the United States Army Corps of Engineers, the United States Coastal Research Program, Sea Grant, and the WHOI Investment in Science Program.

References

Akkermans, R., Cieslik, A., Kamp, L., Trieling, R., Clercx, H., & Van Heijst, G. (2008). The three-dimensional structure of an electromagnetically generated dipolar vortex in a shallow fluid layer. *Physics of Fluids*, *20*(11), 116601. https://doi.org/10.1063/1.3005452

Allen, J. S., Newberger, P. A., & Holman, R. A. (1996). Nonlinear shear instabilities of alongshore currents on plane beaches. *Journal of Fluid Mechanics*, *310*, 181–213. https://doi.org/10.1017/S0022112096001772

Apotsos, A., Raubenheimer, B., Elgar, S., & Guza, R. (2008). Wave-driven setup and alongshore flows observed onshore of a submarine canyon. *Journal of Geophysical Research*, *113*(C7), C07025. https://doi.org/10.1029/2007jc004514

Boehm, A. B., Ismail, N. S., Sassoubre, L. M., & Andruszkiewicz, E. A. (2017). Oceans in Peril: Grand challenges in applied water quality research for the 21st century. *Environmental Engineering Science*, *34*(1), 3–15. https://doi.org/10.1089/ees.2015.0252

Boehm, F. R., Sandrini-Neto, L., Moens, T., & da Cunha Lana, P. (2016). Sewage input reduces the consumption of rhizophora mangle propagules by crabs in a subtropical mangrove system. *Marine Environmental Research*, *122*, 23–32. https://doi.org/10.1016/j.marenvres.2016.09.003

Boffetta, G., & Ecke, R. E. (2012). Two-dimensional turbulence. *Annual Review of Fluid Mechanics*, *44*(1), 427–451. https://doi.org/10.1146/annurev-fluid-120710-101240

Bowen, A. J., & Holman, R. A. (1989). Shear instabilities of the mean longshore current: 1. Theory. *Journal of Geophysical Research*, *94*(C12), 18023–18030. https://doi.org/10.1029/JC094iC12p18023

Bowen, A. J., Inman, D. L., & Simmons, V. P. (1968). Wave 'set-down' and set-Up. *Journal of Geophysical Research*, *73*(8), 2569–2577. https://doi.org/10.1029/JB073i008p02569

Bühler, O., & Jacobson, T. E. (2001). Wave-driven currents and vortex dynamics on barred beaches. *Journal of Fluid Mechanics*, *449*, 313–339. https://doi.org/10.1017/S0022112001006322

Castelle, B., Scott, T., Brander, R., & McCarroll, R. (2016). Rip current types, circulation and hazard. *Earth-Science Reviews*, *163*, 1–21. https://doi.org/10.1016/j.earscirev.2016.09.008

Clark, D. B., Elgar, S., & Raubenheimer, B. (2012). Vorticity generation by short-crested wave breaking. *Geophysical Research Letters*, *39*(24), L24604. https://doi.org/10.1029/2012GL054034

Clark, D. B., Feddersen, F., & Guza, R. T. (2010). Cross-shore surfzone tracer dispersion in an alongshore current. *Journal of Geophysical Research*, *115*(C10), C10035. https://doi.org/10.1029/2009JC005683

Clark, D. B., Feddersen, F., & Guza, R. T. (2011). Modeling surf zone tracer plumes: 2. Transport and dispersion. *Journal of Geophysical Research*, *116*(C11), C11028. https://doi.org/10.1029/2011JC007211

Dalrymple, R. A., MacMahan, J. H., Reniers, A. J., & Nelko, V. (2011). Rip currents. *Annual Review of Fluid Mechanics*, *43*(1), 551–581. https://doi.org/10.1146/annurev-fluid-122109-160733

de Bakker, A. T. M., Tissier, M. F. S., & Ruessink, B. G. (2016). Beach steepness effects on nonlinear infragravity-wave interactions: A numerical study. *Journal of Geophysical Research: Oceans*, *121*(1), 554–570. https://doi.org/10.1002/2015JC011268

Derakhti, M., Kirby, J. T., Shi, F., & Ma, G. (2016). Nhwave: Consistent boundary conditions and turbulence modeling. *Ocean Modelling*, *106*, 121–130. https://doi.org/10.1016/j.ocemod.2016.09.002

Elgar, S., & Raubenheimer, B. (2020). Field evidence of inverse energy cascades in the surf zone. *Journal of Physical Oceanography*, *50*, 2315–2321. https://doi.org/10.1175/JPO-D-19-0327.1

Elgar, S., Raubenheimer, B., Clark, D. B., & Moulton, M. (2019). Extremely low frequency (0.1 to 1.0 mHz) surf zone currents. *Geophysical Research Letters*, *46*(3), 1531–1536. https://doi.org/10.1029/2018GL081106

Elgar, S., Raubenheimer, B., & Guza, R. T. (2005). Quality control of acoustic Doppler velocimeter data in the surf zone. *Measurement Science and Technology*, *16*(10), 1889–1893. https://doi.org/10.1088/0957-0233/16/10/002

Feddersen, F. (2012). Scaling surf zone turbulence. *Geophysical Research Letters*, *39*(18), L18613. https://doi.org/10.1029/2012gl052970

Feddersen, F. (2014). The generation of surf zone eddies in a strong alongshore current. *Journal of Physical Oceanography*, *44*(2), 600–617. https://doi.org/10.1175/JPO-D-13-051.1

Feddersen, F., Clark, D. B., & Guza, R. T. (2011). Modeling surf zone tracer plumes: 1. Waves, mean currents, and low-frequency eddies. *Journal of Geophysical Research*, *116*(C11), C11027. https://doi.org/10.1029/2011JC007210

Feddersen, F., & Guza, R. (2003). Observations of nearshore circulation: Alongshore uniformity, *Journal of Geophysical Research*, *108*(C1), 6–1. https://doi.org/10.1029/2001jc001293

Feddersen, F., Guza, R. T., Elgar, S., & Herbers, T. H. C. (1998). Alongshore momentum balances in the nearshore. *Journal of Geophysical Research*, *103*(C8), 15667–15676. https://doi.org/10.1029/98JC01270

Feddersen, F., & Trowbridge, J. (2005). The effect of wave breaking on surf-zone turbulence and alongshore currents: A modeling study. *Journal of Physical Oceanography*, *35*(11), 2187–2203. https://doi.org/10.1175/jpo2800.1

Garcez-Faria, A. F., Thornton, E. B., Lippmann, T. C., & Stanton, T. P. (2000). Undertow over a barred beach. *Journal of Geophysical Research*, *105*(C7), 16999–17010. https://doi.org/10.1029/2000JC900084

Garcez-Faria, A. F., Thornton, E. B., Stanton, T. P., Soares, C. V., & Lippmannv, T. C. (1998). Vertical profiles of longshore currents and related bed shear stress and bottom roughness. *Journal of Geophysical Research*, *103*(C2), 3217–3232. https://doi.org/10.1029/97JC02265

Geiman, J. D., & Kirby, J. T. (2013). Unforced oscillation of rip-current vortex cells. *Journal of Physical Oceanography*, *43*(3), 477–497. https://doi.org/10.1175/JPO-D-11-0164.1

Gomes, E. R., Mulligan, R. P., Brodie, K. L., & McNinch, J. E. (2016). Bathymetric control on the spatial distribution of wave breaking in the surf zone of a natural beach. *Coastal Engineering*, *116*, 180–194. https://doi.org/10.1016/j.coastaleng.2016.06.012

Guza, R. T., & Thornton, E. B. (1980). Local and shoaled comparisons of sea surface elevations, pressures, and velocities. *Journal of Geophysical Research*, *85*(C3), 1524–1530. https://doi.org/10.1029/JC085iC03p01524

Haller, M. C., & Dalrymple, R. A. (2001). Rip current instabilities. *Journal of Fluid Mechanics*, *433*, 161–192. https://doi.org/10.1017/S0022112000003414

Haller, M. C., Putrevu, U., Oltman-Shay, J., & Dalrymple, R. A. (1999). Wave group forcing of low frequency surf zone motion. *Coastal Engineering Journal*, *41*(02), 121–136. https://doi.org/10.1142/s0578563499000085

Hally-Rosendahl, K., & Feddersen, F. (2016). Modeling surfzone to inner-shelf tracer exchange. *Journal of Geophysical Research: Oceans*, *121*(6), 4007–4025. https://doi.org/10.1002/2015JC011530

Hannan, E. (1970). Multiple time series (pp. 536). Wiley.

Hansen, J. E., Raubenheimer, B., List, J. H., & Elgar, S. (2015). Modeled alongshore circulation and force balances onshore of a submarine canyon. *Journal of Geophysical Research: Oceans*, *120*(3), 1887–1903. https://doi.org/10.1002/2014jc010555

Henderson, S. M., Arnold, J., Özkan-Haller, H. T., & Solovitz, S. A. (2017). Depth dependence of nearshore currents and eddies. *Journal of Geophysical Research: Oceans*, *122*(11), 9004–9031. https://doi.org/10.1002/2016JC012349

Hsu, T.-J., Elgar, S., & Guza, R. (2006). Wave-induced sediment transport and onshore sandbar migration. *Coastal Engineering*, *53*(10), 817–824. https://doi.org/10.1016/j.coastaleng.2006.04.003

Kraichnan, R. H. (1967). Inertial ranges in two-dimensional turbulence. *The Physics of Fluids*, *10*(7), 1417–1423. https://doi.org/10.1063/1.1762301

Kuik, A., Van Vledder, G. P., & Holthuijsen, L. (1988). A method for the routine analysis of pitch-and-roll buoy wave data. *Journal of Physical Oceanography*, *18*(7), 1020–1034. https://doi.org/10.1175/1520-0485(1988)018<1020:amftra>2.0.co;2

Kumar, N., & Feddersen, F. (2017). The effect of stokes drift and transient rip currents on the inner shelf. Part I: No stratification. *Journal of Physical Oceanography*, *47*(1), 227–241. https://doi.org/10.1175/JPO-D-16-0076.1

Kumar, N., Voulgaris, G., Warner, J. C., & Olabarrieta, M. (2012). Implementation of the vortex force formalism in the coupled ocean-atmosphere-wave-sediment transport (COAWST) modeling system for inner shelf and surf zone applications. *Ocean Modelling*, *47*, 65–95. https://doi.org/10.1016/j.ocemod.2012.01.003

Lam, D. C. L., & Simpson, R. B. (1976). Centered differencing and the box scheme for diffusion convection problems. *Journal of Computational Physics*, *22*(4), 486–500. https://doi.org/10.1016/0021-9991(76)90045-0

Launder, B. E., & Spalding, D. B. (1983). The numerical computation of turbulent flows. In Numerical prediction of flow, heat transfer, turbulence and combustion (pp. 96–116), Elsevier. https://doi.org/10.1016/b978-0-08-030937-8.50016-7

Lentz, S. J., & Fewings, M. R. (2012). The wind-and wave-driven inner-shelf circulation. *Annual review of marine science*, *4*, 317–343. https://doi.org/10.1146/annurev-marine-120709-142745

Lippmann, T. C., & Bowen, A. J. (2016). The vertical structure of low-frequency motions in the nearshore. Part II: Theory. *Journal of Physical Oceanography*, *46*(12), 3713–3727. https://doi.org/10.1175/JPO-D-16-0015.1

Lippmann, T. C., Herbers, T. H. C., & Thornton, E. B. (1999). Gravity and shear wave contributions to nearshore infragravity motions. *Journal of Physical Oceanography*, *29*(2), 231–239, https://doi.org/10.1175/1520-0485(1999)029<0231:gaswct>2.0.co;2

Lippmann, T. C., Thornton, E. B., & Stanton, T. P. (2016). The vertical structure of low-frequency motions in the nearshore. Part I: Observations. *Journal of Physical Oceanography*, *46*(12), 3695–3711. https://doi.org/10.1175/JPO-D-16-0014.1

Long, J. W., & Özkan Haller, H. T. (2009). Low-frequency characteristics of wave group–forced vortices. *Journal of Geophysical Research*, *114*(C8), C08004. https://doi.org/10.1029/2008JC004894

Longuet-Higgins, M. S. (1970). Longshore currents generated by obliquely incident sea waves: 1. *Journal of Geophysical Research*, *75*(33), 6778–6789. https://doi.org/10.1029/JC075i033p06778

Longuet-Higgins, M. S., & Stewart, R. W. (1964). Radiation stresses in water waves; a physical discussion, with applications. *Deep-Sea Research and Oceanographic Abstracts*, *11*(4), 529–562. https://doi.org/10.1016/0011-7471(64)90001-4

Lynett Patrick, J. (2006). Nearshore wave modeling with high-order Boussinesq-type equations. *Journal of Waterway, Port, Coastal, and Ocean Engineering*, *132*(5), 348–357. https://doi.org/10.1061/(asce)0733-950x(2006)132:5(348)

MacMahan, J. H., Reniers, A. J. H. M., & Thornton, E. B. (2010). Vortical surf zone velocity fluctuations with 0(10) min period. *Journal of Geophysical Research*, *115*(C6), C06007. https://doi.org/10.1029/2009JC005383

MacMahan, J. H., Reniers, A. J. H. M., Thornton, E. B., & Stanton, T. P. (2004). Infragravity rip current pulsations. *Journal of Geophysical Research*, *109*(C1), C01033. https://doi.org/10.1029/2003JC002068

MacMahan, J. H., Thornton, E. B., & Reniers, A. J. H. M. (2006). Rip current review. *Coastal Engineering*, *53*(2), 191–208. https://doi.org/10.1016/j.coastaleng.2005.10.009

Morgan, S. G., Shanks, A. L., MacMahan, J. H., Reniers, A. J., & Feddersen, F. (2018). Planktonic subsidies to surf-zone and intertidal communities. *Annual review of marine science*, *10*, 345–369. https://doi.org/10.1146/annurev-marine-010816-060514

Moulton, M., Elgar, S., Raubenheimer, B., Warner, J. C., & Kumar, N. (2017). Rip currents and alongshore flows in single channels dredged in the surf zone. *Journal of Geophysical Research: Oceans*, *122*(5), 3799–3816. https://doi.org/10.1002/2016JC012222

Newberger, P. A., & Allen, J. S. (2007a). Forcing a three-dimensional, hydrostatic, primitive-equation model for application in the surf zone: 1. Formulation. *Journal of Geophysical Research*, *112*(C8), C08018. https://doi.org/10.1029/2006JC003472

Newberger, P. A., & Allen, J. S. (2007b). Forcing a three-dimensional, hydrostatic, primitive-equation model for application in the surf zone: 2. Application to DUCK94. *Journal of Geophysical Research*, *112*(C8), C08018. https://doi.org/10.1029/2006JC003474

Noyes, T. J., Guza, R., Elgar, S., & Herbers, T. (2004). Field observations of shear waves in the surf zone. *Journal of Geophysical Research*, *109*(C1), C01031. https://doi.org/10.1029/2002JC001761

O'Dea, A., Kumar, N., & Haller, M. C. (2021). Simulations of the surf zone eddy field and cross-shore exchange on a non-idealized bathymetry. *Journal of Geophysical Research: Oceans*, *126*, e2020JC016619. https://doi.org/10.1029/2020JC016619

Oltman-Shay, J., Howd, P. A., & Birkemeier, W. A. (1989). Shear instabilities of the mean longshore current: 2. Field observations. *Journal of Geophysical Research*, *94*(C12), 18031–18042. https://doi.org/10.1029/JC094iC12p18031

Patankar, S. V. (1980). Numerical heat transfer and fluid flow, hemisphere publ (pp. 58). CRC Press.

Peregrine, D. (1998). Surf zone currents. *Surf Zone Currents, Theoretical and Computational Fluid Dynamics*, *10*(1), 295–309. https://doi.org/10.1007/s001620050065
Peregrine, D. H. (1983). Water waves, nonlinear Schrödinger equations and their solutions. *ANZIAM Journal*, *25*(1), 16–43. https://doi.org/10.1017/S0334270000003891
Plant, N. G., Holland, K. T., & Puleo, J. A. (2002). Analysis of the scale of errors in nearshore bathymetric data. *Marine Geology*, *191*(1), 71–86. https://doi.org/10.1016/S0025-3227(02)00497-8
Priestely, M. (1981). Spectral analysis and time series (pp. 890). Academic Press.
Putrevu, U., Oltman-Shay, J., & Svendsen, I. A. (1995). Effect of alongshore nonuniformities on longshore current predictions. *Journal of Geophysical Research*, *100*(C8), 16119–16130. https://doi.org/10.1029/95JC01459
Raubenheimer, B., Guza, R. T., & Elgar, S. (2001). Field observations of wave-driven setdown and setup. *Journal of Geophysical Research*, *106*(C3), 4629–4638. https://doi.org/10.1029/2000JC000572
Reniers, A. J. H. M., MacMahan, J. H., Thornton, E. B., & Stanton, T. P. (2007). Modeling of very low frequency motions during RIPEX. *Journal of Geophysical Research*, *112*(C7), C07013. https://doi.org/10.1029/2005JC003122
Reniers, A. J. H. M., Roelvink, J. A., & Thornton, E. B. (2004). Morphodynamic modeling of an embayed beach under wave group forcing. *Journal of Geophysical Research*, *109*(C1), C01030. https://doi.org/10.1029/2002JC001586
Reniers, A. J. H. M., Thornton, E. B., Stanton, T. P., & Roelvink, J. A. (2004). Vertical flow structure during Sandy Duck: Observations and modeling. *Coastal Engineering*, *51*(3), 237–260. https://doi.org/10.1016/j.coastaleng.2004.02.001
Rijnsdorp, D. P., Ruessink, G., & Zijlema, M. (2015). Infragravity-wave dynamics in a barred coastal region, a numerical study. *Journal of Geophysical Research: Oceans*, *120*(6), 4068–4089. https://doi.org/10.1002/2014JC010450
Rijnsdorp, D. P., Smit, P. B., & Zijlema, M. (2012). Non-hydrostatic modelling of infragravity waves using swash. *Coastal Engineering Proceedings*, *1*(33), 27. https://doi.org/10.9753/icce.v33.currents.27
Rijnsdorp, D. P., Smit, P. B., & Zijlema, M. (2014). Non-hydrostatic modelling of infragravity waves under laboratory conditions. *Coastal Engineering*, *85*, 30–42. https://doi.org/10.1016/j.coastaleng.2013.11.011
Rijnsdorp, D. P., Smit, P. B., Zijlema, M., & Reniers, A. J. H. M. (2017). Efficient non-hydrostatic modelling of 3d wave-induced currents using a subgrid approach. *Ocean Modelling*, *116*, 118–133. https://doi.org/10.1016/j.ocemod.2017.06.012
Rosenfeld, L. (1983). Code-1: Moored array and large-scale data report (pp. 83–23). Woods Hole Oceanographic Institution Tech. Report.
Ruessink, B., Miles, J., Feddersen, F., Guza, R., & Elgar, S. (2001). Modeling the alongshore current on barred beaches. *Journal of Geophysical Research*, *106*(C10), 22451–22463. https://doi.org/10.1029/2000jc000766
Ruju, A., Lara, J. L., & Losada, I. J. (2014). Numerical analysis of run-up oscillations under dissipative conditions. *Coastal Engineering*, *86*, 45–56. https://doi.org/10.1016/j.coastaleng.2014.01.010
Shanks, A. L., Morgan, S. G., MacMahan, J., & Reniers, A. J. H. M. (2010). Surf zone physical and morphological regime as determinants of temporal and spatial variation in larval recruitment. *Journal of Experimental Marine Biology and Ecology*, *392*(1), 140–150. https://doi.org/10.1016/j.jembe.2010.04.018
Simons, R. R., Grass, T. J., & Mansour-Tehrani, M. (1992). Bottom shear stresses in the boundary layers under waves and currents crossing at right angles. *Coastal Engineering Proceedings*, *1*(23). https://doi.org/10.9753/icce.v23.%p
Smagorinsky, J. (1963). General circulation experiments with the primitive equations. *Monthly Weather Review*, *91*(3), 99–164. https://doi.org/10.1175/1520-0493(1963)091<0099:gcewtp>2.3.co;2
Smith, J. A., & Largier, J. L. (1995). Observations of nearshore circulation: Rip currents. *Journal of Geophysical Research*, *100*(C6), 10967–10975. https://doi.org/10.1029/95jc00751
Smith, J. M., Bak, S., Hesser, T., Bryant, M. A., & Massey, C. (2017). Frf wave test bed and bathymetry inversion. *Coastal Engineering Proceedings*, *1*(35), 22. https://doi.org/10.9753/icce.v35.waves.22
Smit, P., Janssen, T., Holthuijsen, L., & Smith, J. (2014). Non-hydrostatic modeling of surf zone wave dynamics. *Coastal Engineering*, *83*, 36–48. https://doi.org/10.1016/j.coastaleng.2013.09.005
Smit, P., Zijlema, M., & Stelling, G. (2013). Depth-induced wave breaking in a non-hydrostatic, near-shore wave model. *Coastal Engineering*, *76*, 1–16. https://doi.org/10.1016/j.coastaleng.2013.01.008
Spydell, M., & Feddersen, F. (2009). Lagrangian drifter dispersion in the surf zone: Directionally spread, normally incident waves. *Journal of Physical Oceanography*, *39*(4), 809–830. https://doi.org/10.1175/2008JPO3892.1
Stive, M. J. F., & Wind, H. G. (1982). A study of radiation stress and set-up in the nearshore region. *Coastal Engineering*, *6*(1), 1–25. https://doi.org/10.1016/0378-3839(82)90012-6
Stoner, N., & Dorfman, M. (2007). Testing the waters: A guide to water quality at vacation beaches. *Natural Resources Defense Council*, *8*, 12.
Suanda, S. H., & Feddersen, F. (2015). A self-similar scaling for cross-shelf exchange driven by transient rip currents. *Geophysical Research Letters*, *42*(13), 5427–5434. https://doi.org/10.1002/2015GL063944
Tabeling, P., Cardoso, O., & Perrin, B. (1990). Chaos in a linear array of vortices. *Journal of Fluid Mechanics*, *213*, 511–530. https://doi.org/10.1017/s0022112090002427
Tissier, M., Bonneton, P., Marche, F., Chazel, F., & Lannes, D. (2012). A new approach to handle wave breaking in fully non-linear Boussinesq models. *Coastal Engineering*, *67*, 54–66. https://doi.org/10.1016/j.coastaleng.2012.04.004
Tonelli, M., & Petti, M. (2010). Finite volume scheme for the solution of 2d extended Boussinesq equations in the surf zone. *Ocean Engineering*, *37*(7), 567–582. https://doi.org/10.1016/j.oceaneng.2010.02.004
Uchiyama, Y., McWilliams, J. C., & Akan, C. (2017). Three-dimensional transient rip currents: Bathymetric excitation of low-frequency intrinsic variability: 3-D TRANSIENT RIP CURRENTS. *Journal of Geophysical Research: Oceans*, *122*(7), 5826–5849. https://doi.org/10.1002/2017JC013005
Uchiyama, Y., McWilliams, J. C., & Shchepetkin, A. F. (2010). Wave–current interaction in an oceanic circulation model with a vortex-force formalism: Application to the surf zone. *Ocean Modelling*, *34*(1), 16–35. https://doi.org/10.1016/j.ocemod.2010.04.002
Visser, P. J. (1986). Wave basin experiments on bottom friction due to current and waves. *Coastal Engineering Proceedings*, *1*(20), 61. https://doi.org/10.9753/icce.v20.%p
Warner, J. C., Armstrong, B., He, R., & Zambon, J. B. (2010). Development of a coupled ocean–Atmosphere–wave–sediment transport (COAWST) modeling system. *Ocean Modelling*, *35*(3), 230–244. https://doi.org/10.1016/j.ocemod.2010.07.010
Zijlema, M., Stelling, G., & Smit, P. (2011). SWASH: An operational public domain code for simulating wave fields and rapidly varied flows in coastal waters. *Coastal Engineering*, *58*(10), 992–1012. https://doi.org/10.1016/j.coastaleng.2011.05.015
Zijlema, M., & Stelling, G. S. (2005). Further experiences with computing non-hydrostatic free-surface flows involving water waves. *International Journal for Numerical Methods in Fluids*, *48*(2), 169–197. https://doi.org/10.1002/fld.821